2015

Aerodynamics, kinematics, and ecology of slow flight in birds

Kristen Elizabeth Crandell

AERODYNAMICS, KINEMATICS, AND ECOLOGY OF SLOW FLIGHT IN BIRDS

By

KRISTEN ELIZABETH CRANDELL

B.A. Lewis & Clark College, Portland, OR, 2009

Dissertation

presented in partial fulfillment of the requirements
for the degree of

Doctor of Philosophy
in Organismal Biology and Ecology

The University of Montana
Missoula, MT

December 2015

Approved by:

Sandy Ross, Dean of The Graduate School
Graduate School

Bret Tobalske, Chair
Division of Biological Sciences

Douglas Emlen
Division of Biological Sciences

Art Woods
Division of Biological Sciences

Andrew Biewener
Department of Organismic and Evolutionary Biology
Harvard University

Sharon Swartz
Department of Ecology and Evolutionary Biology
Brown University

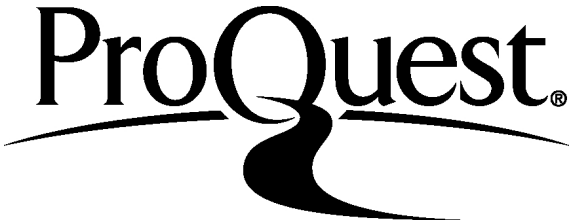

Crandell, Kristen, P.h.D., Fall 2015 Organismal Biology and Ecology

Aerodynamics, kinematics, and ecology of slow flight in birds

Chairperson: Bret W. Tobalske

The overarching goal of my dissertation is to elucidate the force production mechanisms of slow flight in birds. Slow flight is extremely energetically costly per unit time, yet highly important for takeoff and survival in birds. However, at slow speeds it is presently thought that most birds do not produce beneficial aerodynamic forces during the entire wingbeat: instead, they fold or flex their wings during upstroke, prompting the long-standing prediction that the upstroke produces trivial forces. Here, I examined the kinematics, aerodynamics, skeletal drivers, and potential ecological influences of force production in flight. In chapter one, I establish that wings in upstroke posture are capable of producing beneficial aerodynamic forces. Chapter two illustrates diamond doves that keep their wings extended in a "wingtip-reversal" upstroke (at Re=50,000) produce a kinematic and aerodynamic signature similar to the clap-and-peel mechanism previously reported only in insects (Re=8,000). In contrast, zebra finch use a "flexed-wing" upstroke that is aerodynamically inactive. Integrating an XROMM (X-ray Reconstruction of Moving Morphology) study of pigeons and starlings in chapter three, I demonstrate that both upstroke styles have similar skeletal kinematics (with a few notable exceptions), but the timing and extent of motion differs. Lastly, chapter four faces birds with an ecologically relevant task: transitioning from a compliant substrate reduces initial flight velocities, and birds do not appear to modulate force production to compensate. Collectively, I reveal that the clap and fling mechanism utilized by many species is a wing motion that is aerodynamically beneficial and largely due to an interaction of the skeletal elements. These four chapters illuminate an energetically costly and ecologically relevant period of flight.

Aerodynamics, kinematics, and ecology of slow flight in birds

To initiate and end locomotion, an animal must accelerate from rest and decelerate to stop. Most studies of movement have focused on steady-state locomotion, during which the organism moves at a constant pace (Dickinson et al., 2000). In the natural world, this type of locomotion may be the exception to the norm; animals are constantly starting and stopping. For many organisms, these transitional phases may be the most crucial: to escape predation, impress a potential mate, and move between resources. Thus, the ability to change velocity is as important as the ability to maintain steady velocity in the animal world.

Acceleration (and steady-state locomotion) in terrestrial environments can be conveniently divided in to two parts for vertebrates: the stance and swing phases. During the stance phase, the limb directly applies a force to the environment (i.e., the ground). The swing phase occurs as the limb is lifted off the ground and cycled forward to prepare for the next stance phase. Unsurprisingly, this phase is not directly producing any useful forces, because it is not in contact with the ground. In contrast, animals in a fluid environment (air or water) are constantly in direct contact with their environment. This continuous contact may provide an opportunity to produce useful forces during the traditional terrestrial swing phase.

Birds are able to capitalize on the swing phase, the upstroke, during fast flight: they produce a force to offset bodyweight (lift). In contrast, the functional significance of the upstroke during slow flight is unknown. The critical difference between these two speeds has to do with a continuous property of air: as the speed of the object in air increases, so too does the number of air molecules with which the

object (such as a wing) interacts. Thus, during slow flight a majority of the aerodynamic power required to fly is expended to support the animal's weight, while during fast flight power requirements for weight support (known as induced power) are much lower. This implies that a bird is operating near its aerodynamic limits during slow flight. Even so, slow flight is a crucial phase for a bird. In order to fly from a standstill, a bird must accelerate through a slow phase to reach a comfortable cruising speed. Given that slow, accelerating flight is energetically costly, near aerodynamic limits, and likely under selective pressures for brevity, I predict that birds should use mechanisms to rapidly accelerate following takeoff. One such method a bird may be able to accomplish this rapid acceleration, without an added energetic cost, may be during upstroke.

During slow flight, birds produce one of two upstroke styles: the wingtip-reversal upstroke, wherein the wing is extended and the hand wing goes through significant supination and pronation, or the flexed-wing upstroke, wherein the wing is flexed toward the body, and extended to initiate the next downstroke. It was first proposed by Marey in 1890 (Marey, 1890) that the tip-reversal upstroke may be aerodynamically active. Various studies hence have substantiated this claim (Brown, 1953; Hedrick and Biewener, 2007; Lorenz, 1933; Ros et al., 2011) yet the aerodynamic and internal mechanism remains unknown.

The overarching goal of my dissertation is to elucidate the force production mechanisms of slow flight in birds. Herein, I address the aerodynamics, kinematics, skeletal drivers, and potential ecological influences of force production in flight. The first chapter models the aerodynamic force production of a wing in upstroke and

downstroke posture, indicating that the posture of tip-reversal upstroke is capable of producing significant aerodynamic forces. The second chapter examines force production *in vivo*. I establish that the tip-reversal upstroke capitalizes on a time-dependent "clap and peel" mechanism, wherein the left and right wings interact at the upstroke to downstroke transition to produce additional circulation greater than that which is generated in a non clap-and-peel transition. In contrast, the flexed wing upstroke produces minimal induced momentum to the wake, and is largely aerodynamically inactive. The third chapter examines the underlying mechanical driver of these mechanisms via an XROMM (X-ray Reconstruction of Moving Morphology) reconstruction of skeletal kinematics. Here, I establish that both upstroke styles have generally similar skeletal kinematics (with a few notable exceptions), but the timing and extent of each motion differs to produce drastically different external wing motion. Lastly, I explore the ability of birds to modulate the forces and kinematics observed in the first three chapters when faced with an ecologically-relevant task. Transitioning from a compliant substrate reduces initial flight velocity, and birds to not appear to modulate force production to compensate. Together, these four chapters help illuminate an energetically costly and ecologically relevant period of flight.

References:

Brown, R. H. J. (1953). The flight of birds 2. Wing function in relation to flight speed. *Journal of Experimental Biology* **30**, 90-103.

Dickinson, M. H., Farley, C. T., Full, R. J., Koehl, M. A. R., Kram, R. and Lehman, S. (2000). How animals move: An integrative view. *Science* **288**, 100-106.

Hedrick, T. L. and Biewener, A. A. (2007). Low speed maneuvering flight of the rose-breasted cockatoo (Eolophus roseicapillus). I. Kinematic and neuromuscular control of turning. *Journal of Experimental Biology* **210**, 1897-1911.

Lorenz, K. (1933). Beobachtetes über das Fliegen der Vögel und über die Beziehungen der Flügel-und Steuerform zur Art des Fluges. *Journal of Ornithology* **81**, 107-236.

Marey, E. (1890). Locomotion Dans L'air, Vol. Des Oiseaux. In *Le mouvement*. Paris, France.

Ros, I. G., Bassman, L. C., Badger, M. A., Pierson, A. N. and Biewener, A. A. (2011). Pigeons steer like helicopters and generate down- and upstroke lift during low speed turns. *Proceedings of the National Academy of Sciences of the United States of America* **108**, 19990-19995.

The Journal of Experimental Biology 214, 1867-1873

doi:10.1242/jeb.051342

RESEARCH ARTICLE

Aerodynamics of tip-reversal upstroke in a revolving pigeon wing

Kristen E. Crandell* and Bret W. Tobalske

Field Research Station at Fort Missoula, Division of Biological Sciences, University of Montana, Missoula, MT 59812, USA

*Author for correspondence (kristen.crandell@umontana.edu)

Accepted 28 February 2011

SUMMARY

During slow flight, bird species vary in their upstroke kinematics using either a 'flexed wing' or a distally supinated 'tip-reversal' upstroke. Two hypotheses have been presented concerning the function of the tip-reversal upstroke. The first is that this behavior is aerodynamically inactive and serves to minimize drag. The second is that the tip-reversal upstroke is capable of producing significant aerodynamic forces. Here, we explored the aerodynamic capabilities of the tip-reversal upstroke using a well-established propeller method. Rock dove (*Columba livia, N*=3) wings were spread and dried in postures characteristic of either mid-upstroke or mid-downstroke and spun at *in vivo* Reynolds numbers to simulate forces experienced during slow flight. We compared 3D wing shape for the propeller and *in vivo* kinematics, and found reasonable kinematic agreement between methods (mean differences 6.4% of wing length). We found that the wing in the upstroke posture is capable of producing substantial aerodynamic forces. At *in vivo* angles of attack (66 deg at mid-upstroke, 46 deg at mid-downstroke), the upstroke wings averaged for three birds produced a lift-to-drag ratio of 0.91, and the downstroke wings produced a lift-to-drag ratio of 3.33. Peak lift-to-drag ratio was 2.5 for upstroke and 6.3 for downstroke. Our estimates of total force production during each half-stroke suggest that downstroke produces a force that supports 115% of bodyweight, and during upstroke a forward-directed force (thrust) is produced at 36% of body weight.

Key words: upstroke, propeller model, pigeon, *Columba livia*, flight, wing, lift, drag, tip-reversal.

INTRODUCTION

In almost all birds flight plays a crucial role in survival, whether in foraging, attracting mates, defending territories, migrating or avoiding predators. In order to accomplish all of these tasks in flight, birds must first take off and accelerate to the appropriate speed. During this acceleration, flying birds appear to have two unique patterns of wing kinematics, associated with wing morphology. The first group fully flexes their wings on the upstroke and has low aspect ratio, rounded wings. The second group uses a 'tip-reversal' upstroke, in which the distal wing is heavily supinated, and includes birds with high aspect ratio, pointed wingtips (Brown, 1963; Tobalske, 2000; Tobalske et al., 2003). A notable exception to this pattern is seen in a group of birds designed for explosive take-off, *Phasianidae*, which have rounded, low aspect ratio wings but a prominent tip-reversal upstroke (Tobalske and Dial, 2000).

The functional significance of the tip-reversal upstroke has been debated for nearly a century. Early flow-visualization evidence suggested that the tip-reversal upstroke is aerodynamically inactive, meaning that it does not produce lift for weight support or thrust (Spedding et al., 1984; Spedding, 1986). However, this is unlikely given dramatic differences in wing kinematics (Brown, 1953; Tobalske and Dial, 1996) between upstroke styles, and observed increases in body acceleration during the upstroke (Brown, 1963; Aldridge, 1987). These early measures of body acceleration do not account for wing inertia in calculating center of mass acceleration, and thus may not accurately reflect performance. Recent evidence for an active upstroke is found in feather loading during the upstroke, indicating a net force directed anteriorly to the bird (Corning and Biewener, 1998), and significant differential pressure on the surfaces of the wing during upstroke through take-off and landing (Usherwood et al., 2005). Similarly, an analysis of instantaneous force changes as measured by accelerometers indicates that the tip-reversal upstroke in a cockatiel (*Nymphicus hollandicus*) provides 14% the lift of downstroke (Hedrick et al., 2004). If the upstroke provides a portion of the lift or thrust forces necessary for flight, birds that exhibit a tip-reversal upstroke may have a large advantage during slow flight in comparison to birds that flex their wings on the upstroke. Slow flight is energetically costly (Rayner, 1995); induced drag is high, so much of the power required to fly slowly is used to support the animal's weight (Ellington, 1991). Thus, we expect that animals should capitalize on mechanisms that allow them to rapidly accelerate to speeds that require less power output. Therefore, we predict that a tip-reversal upstroke will be aerodynamically active.

Here, we tested for an aerodynamic function of the upstroke in the rock dove (*Columba livia*, Gmelin 1789, hereafter 'pigeon') using a well-established propeller method (Usherwood and Ellington, 2002a; Usherwood and Ellington, 2002b) that has thus far only been used to model wing function during mid-downstroke (Usherwood and Ellington, 2002a; Usherwood and Ellington, 2002b; Altshuler et al., 2004; Usherwood, 2009). We used *in vivo* kinematics to model the posture of spread wings and to determine the Reynolds number estimated from wingtip angular velocity. We then directly measured lift and drag by mounting the dried-wing propellers on a force plate.

MATERIALS AND METHODS

Kinematics

A captive-bred pigeon was housed in an outdoor aviary at the Field Research Station at Fort Missoula. The bird was trained to fly

between horizontal platforms positioned approximately 2 m apart. Prior to kinematic recordings, the bird was marked with black permanent marker at the shoulder, wrist and each primary feather tip, and at three locations on the ventral surface of the body for later digitization. All care and experimental procedures were approved by the University of Montana IACUC.

We recorded the flight of the pigeon using four high-speed cameras: one Photron SA-3 (Photron USA Inc., San Diego, CA, USA), two Photron 1024 PCI and one Fastec Troubleshooter (Fastec Imaging, San Diego, CA, USA), synchronized using a transistor–transistor logic (TTL)-pulse. One camera was placed dorsally and behind the flight path, two were ventrally placed behind and in front of the flight path, and a fourth was placed horizontal to the bird in front of the flight path. Video recordings were made at 1000 Hz with a shutter speed of 1/10,000 s.

To analyze the kinematic data, we recorded a 36-point calibration volume (approximately 30×45×80 cm) for the space between the platforms. A direct linear transformation converted the four camera views into 3D coordinates (MATLAB R2010a, The MathWorks Inc., Natick, MA, USA) (Hedrick, 2008). Markers along the wings were digitized from recorded images to obtain 3D wing kinematics. The third wingbeat cycle following take-off was used.

We performed subsequent analysis using custom scripts in MATLAB. Angular velocity (rad s^{-1}) of the hand wing was calculated by determining a central position in three dimensions between the wrist, the 10th primary feather and the 1st secondary feather, to represent the total hand wing. We then determined the velocity vector of the hand wing, relative to the shoulder of the bird. To determine the angle of attack (α, deg) in global coordinates (accounting for translation), we measured the angle between the velocity vector of the hand wing and the vector normal to the hand-wing plane, and subtracted this from 90 deg.

Morphology

Wings were removed from three deceased birds (body mass, 446±69 g) and dried in a low temperature oven at 40°C for 1 week. We obtained paired models for each individual, with one wing in mid-upstroke posture and the other in mid-downstroke posture. Each wing was mounted on a brass rod at the proximal edge of the head of the humerus to create a one-blade propeller, with the rod acting as a counterweight (Fig. 1). Wings were photographed and analyzed in ImageJ (v1.43u, National Institutes of Health, Bethesda, MA, USA) and MATLAB to determine wing length and the first, second and third moments of area [following Usherwood and Ellington (Usherwood and Ellington, 2002b)] (Table 1). The second moment of area directly correlates with aerodynamic force, and the third moment with torque (Weis-Fogh, 1973). Thus, these two measurements allow us to account for slight differences in wing shape between birds when calculating mean vertical and horizontal forces (Eqns 1 and 2).

Propeller

Each wing was spun once at each angle of attack (α), in increments of approximately 10 deg from –10 to 90 deg. Wings were mounted to a brushless DC motor (NEMA 34 motor, Anaheim Automation Inc., Anaheim, CA, USA), and controlled with an Anaheim Automation driver and power supply (DCL 601USB, MBC 12101 and PSA 40V8A), with SMC60WIN software (v. 2.01). Revolutions per minute (r.p.m.) values were based on the mean angular velocity of the wingtip during the middle third of each half-stroke, as determined from *in vivo* kinematics for upstroke and downstroke. The third wingbeat following take-off of the live pigeon had an angular velocity of 69 rad s^{-1} for the mid-third of downstroke, and 96 rad s^{-1} for the mid-third of upstroke, which translated into 376 and 572 r.p.m., respectively.

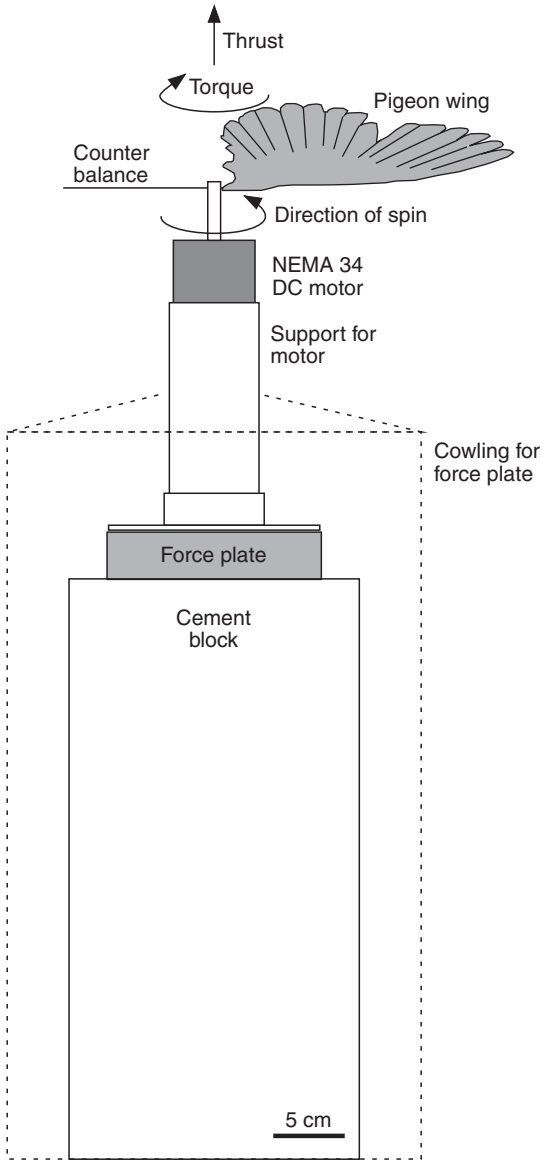

Fig. 1. The propeller setup.

The propeller shaft was constructed to allow the insertion and manipulation of the brass rod for easy rotation of the wing over a full range of α. We measured α as the acute angle between horizontal and a line described by two points on the wing: midway between the wrist, tip of the 10th primary feather and the tip of the 1st primary feather. We visualized these points using a digital video camera (Photron SA-3 using PFV 3.1.8 software) that was placed horizontal to the wing. We measured α before spinning the wing and during rotation, both to account for deformation due to aerodynamic loading of the wing and to report active α for final analysis. Active α was on average 2±3 deg less than static α.

The wings were mounted so that induced velocities in the wake would generally be directed upwards, away from the force plate. For the downstroke posture, for example, this meant the wing was mounted with its ventral surface facing upwards when α>0 deg. For

upstroke posture wings, the secondaries contacted the motor when $\alpha<50$ deg, so we oriented the wing so that the ventral surface faced downwards. The aerodynamic contributions of the counterweight were accounted for by spinning a rod with double the length of the counterweight, centered on the propeller shaft, at appropriate r.p.m. The resulting measurements were halved and subtracted from observed wing values.

We used a custom-built force plate (15×15 cm, Bertec Corp., Columbus, OH, USA) to measure vertical force along the *z*-axis and torque about the *z*-axis due to drag (Usherwood, 2009). The force plate featured a known conversion of 10,000 mN V^{-1} for force and 800 mN V^{-1} for torque. Voltage output from the force plate was converted and amplified with a digital gain of 5× using a Bertec model M6810 amplifier. We imported these data to a computer using an ADInstruments PowerLab 8SP A/D converter sampling at 1000 Hz and Chart v5.2 software using a 1 Hz low-pass digital filter (ADInstruments Inc., Colorado Springs, CO, USA). A cardboard cowling (shield) surrounded the base of the motor and the force plate in order to isolate the force plate from air velocities induced by the spinning wings (Fig. 1).

Wing shape during spinning *versus* flight

To compare deflection of primary feathers during model rotation with *in vivo* wing shape, we used 3D video recording and analysis on the propeller model (see 'Kinematics', above). We videotaped the upstroke and downstroke wing models when spinning with α comparable to *in vivo* measurements (66 deg for upstroke, 46 deg for downstroke wings). To compare wing shape between the live bird and propeller, digitized points were standardized to a right-hand rule, local coordinate system rooted at the wrist, with the *x*-axis extending through the 10th primary feather. Conversion from global to local coordinates was accomplished using a series of Euler angle transformations.

We assessed variation for each feather between a model wing (Fig. 2, blue lines) and live animal (red lines) in both the proximal–distal and ventral–dorsal axes. Feather offset was measured as the linear distance in three dimensions from each primary feather tip to its corresponding feather in the live bird, and normalized by dividing by the wing length (Fig. 2). Feathers in upstroke-postured wings differed from *in vivo* feathers by 1.96±0.97 cm or 6.05±2.75% of wing length. Downstroke posture wings differed by 2.02±0.91 cm or 6.78±3.06% of wing length.

Determining coefficients of lift and drag

Data from the force plate were converted to the coefficient of lift or drag by a series of equations presented by Usherwood and Ellington (Usherwood and Ellington, 2002a). The mean vertical force reported by the force plate ($\mathbf{F}_v$, mN) was converted to the mean vertical force coefficient (C_v):

$$C_v = \frac{2\mathbf{F}_v}{\rho S_2 \Omega^2}\ , \qquad (1)$$

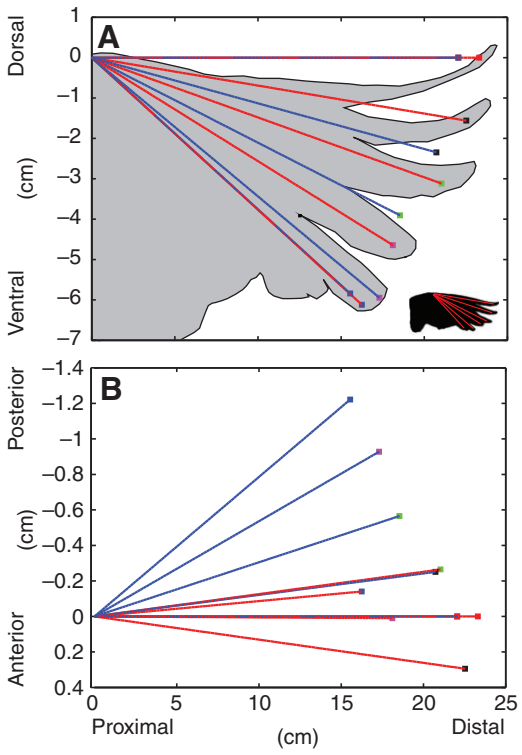

Fig. 2. A comparison of *in vivo* and propeller wing feather deflection at a 66 deg angle of attack for a wing during mid-upstroke. Live bird and propeller data were normalized to a standard coordinate system along the 10th primary feather. Each line represents a position vector from the wrist base to the tip of each primary feather (colored squares). The live bird is shown in red, the upstroke wing model from one bird in blue.
(A) Proximal–distal and ventral–dorsal axis, with feather outlines in gray.
(B) Proximal–distal and anterior–posterior axis.

where ρ is the air density (1.07 kg m^{-3}, in Missoula, MT, USA) during the experiments, S_2 is the second moment of area (Table 1) and Ω is the angular velocity (rad s^{-1}). Then, we converted the mean torque (Q, mN m) about the *z*-axis of the plate to a horizontal force coefficient (C_h):

$$C_h = \frac{2Q}{\rho S_3 \Omega^2}\ , \qquad (2)$$

where S_3 is the third moment of area.

Using both of these values, we determined the dimensionless coefficient of lift (C_L) and drag (C_D), using a value for the local downwash angle (ε) determined geometrically assuming a triangular distribution of induced velocity along the wing (Usherwood and Ellington, 2002a). This distribution has been confirmed for the

Table 1. Morphometrics for pigeon (*Columba livia*) wings used for propeller model (*N*=3)

	Downstroke	Upstroke
Wing length (*R*; m)	3.14E–01±2.47E–02	2.43E–01±1.09E–02
Wing Area (*S*; m^2)	3.35E–02±4.02E–03	2.05E–02±2.92E–03
Second moment of wing area (S_2; m^4)	8.37E–04±3.22E–04	2.36E–04±2.21E–05
Third moment of wing area (S_3; m^5)	1.76E–04±8.07E–05	3.54E–05±3.66E–06

For each bird, the right wing was positioned in upstroke posture, the left in downstroke.

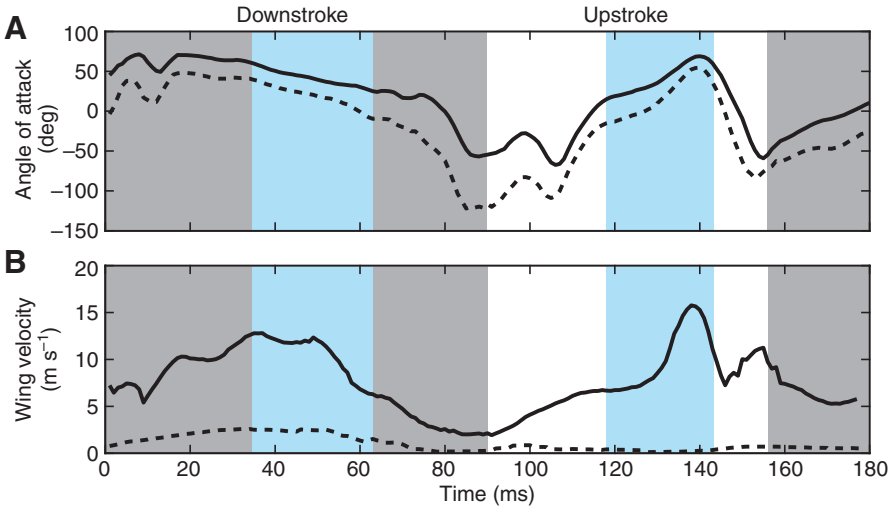

Fig. 3. Kinematic parameters extracted from the third wingbeat cycle; downstroke is shaded, and times approximated by the propeller model are highlighted in blue. (A) Geometric angle of attack (α, deg): α is shown by the solid line, α accounting for the estimated induced velocity is shown by the dashed line (see Discussion). (B) Wing velocity ($m\,s^{-1}$) for a full wingbeat cycle: wingtip is shown by the solid line, wrist is shown by the dashed line.

propeller model with chukar partridge (*Alectoris chukar*) wings using particle image velocimetry (PIV) (Heers et al., 2011). Thus, C_L was:

$$C_L = (C_v\cos\varepsilon + C_h\sin\varepsilon)\,(\cos\varepsilon)^{-2} \quad (3)$$

and C_D was:

$$C_D = (C_h\cos\varepsilon - C_v\sin\varepsilon)\,(\cos\varepsilon)^{-2}\,. \quad (4)$$

While *in vivo* upstroke kinematics qualitatively differ from downstroke kinematics, the tip-reversal upstroke rotates around the wrist, where the pigeon averages an angular velocity of only $6.5\,rad\,s^{-1}$. Thus, by positioning the wrist over the axis of rotation in our propeller model, we can assume a constant angular velocity along the hand wing during upstroke, and use the above calculations for both upstroke and downstroke wings.

Estimating *in vivo* performance

Combining *in vivo* kinematics with force coefficients extracted from the propeller model allows us to consider the force production of a pigeon during the third wingbeat cycle following take-off using coefficients measured with the propeller. First, assuming a hovering case, we can calculate lift (**L**) as:

$$\mathbf{L} = \tfrac{1}{2}\rho V^2 C_L S_2 \quad (5)$$

and drag (**D**) as:

$$\mathbf{D} = \tfrac{1}{2}\rho V^2 C_D S_2\,; \quad (6)$$

then, the resultant force ($\mathbf{F_R}$) is calculated as:

$$\mathbf{F_R} = \sqrt{(\mathbf{L}^2 + \mathbf{D}^2)}\,. \quad (7)$$

However, because the bird is moving forward, we must account for both translational velocity (Dickinson and Dickinson, 2004) and Ω along the wing (Ω_r). We used a blade element analysis (Osborne, 1951) and expanded Eqn 1 to find the vertical force ($\mathbf{F_v}$):

$$\mathbf{F_v} = \rho C_v \int_{r=0}^{R} (\Omega_r\, r + V_T)^2\, c_r\, dr\,, \quad (8)$$

where c is the chord length and V_T is the translational velocity of the wing accounting for stroke plane angle. We estimated Ω_r directly from kinematic data by dividing the leading edge (defined by a line between shoulder, wrist, and wingtip) into equal segments and taking the Ω_r for mean mid-stroke. Wing velocity increased toward the distal wingtip (Fig. 3B, wrist and wingtip). For upstroke, these calculations considered only the hand wing, as the proximal wing is flexed near the body with a low velocity (Fig. 3B, dashed line), and thus was assumed to be aerodynamically inactive. We substituted C_h for C_v in Eqn 8 to estimate $\mathbf{F_h}$. The resultant of these forces then estimates net force production.

Data analysis

We computed polars of mean C_L among the three birds sampled as a function of mean C_D as well as mean lift-to-drag ratio (C_L:C_D) as a function of α. To accomplish this, we first interpolated 95 points for C_L and C_D, to account for subtle differences in α measured between wing samples. We calculated between α=–10 deg and α=85 deg using IGOR Pro (v. 6.01, Wavemetrics, Inc., Beaverton, OR, USA). We then computed a mean and standard deviation among birds for each point in the interpolated series. Herein, we report these means ± s.d.

RESULTS

Kinematics

The third wingbeat cycle following take-off was used in analyses. Angle of attack (Fig. 3A) ranged from 72 deg at the start of downstroke to –68 deg during upstroke. Mean downstroke α=48 deg, and during the mid-third of downstroke (Fig. 3A, blue) mean α=46 deg. Mean upstroke α=–2 deg, but it ranged from –68 to 71 deg. The mean α during the mid-third of upstroke (Fig. 3A, blue) was α=66 deg. Angular velocity (Ω) for the mid-third of downstroke was $69\,rad\,s^{-1}$, and for the mid-third of upstroke Ω=$96\,rad\,s^{-1}$. Tangential velocity of the wingtip varied throughout the stroke cycle, averaging $10.1\,m\,s^{-1}$ for mid-downstroke and $8.9\,m\,s^{-1}$ for upstroke (Fig. 3B). Maximum wingtip velocity for downstroke was $12.8\,m\,s^{-1}$; for upstroke it was $15.3\,m\,s^{-1}$. Velocities along the wing measured from proximal to distal grew to a maximum at the wingtip (Fig. 3B, wrist and wingtip). However, during upstroke the proximal wing velocity remained low, likely due to being flexed against the body.

Propeller force coefficients

Coefficients for lift and drag plotted against α for all three birds revealed substantial lift production by the upstroke wings, with a general pattern that followed that of downstroke (Fig. 4). Upstroke-posture wings had a maximum C_L of 1.42±0.08 at α=53.8 deg (Fig. 4A), and downstroke wings had a maximum C_L of 1.77±0.43 at α=60.8 deg (Fig. 4C). For upstroke wings, the minimum mean

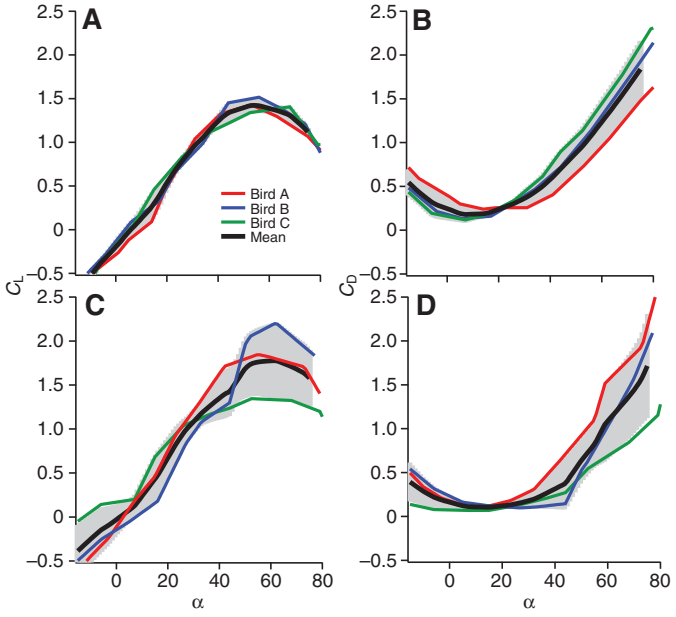

Fig. 4. Aerodynamic force coefficients for wing in upstroke (A,B) and downstroke (C,D) postures with reference to angle of attack (α). *N*=3 birds. Mean among birds is shown by the bold black line, and the shaded area represents ±s.d.

C_D was 0.18±0.09 at α=7.3 deg (Fig. 4B) while for downstroke wings mean C_D was 0.10±0.03 at α=14.3 deg (Fig. 4D).

A diagram of C_L as a function of C_D revealed that the shape of the C_L:C_D polars was similar between wing postures (Fig. 5A). The difference in values appears to caused by both a lower C_L and a higher C_D for upstroke wings, due to the minimum and maximum values seen in Fig. 4. The slopes of the C_L:C_D polar for upstroke and downstroke wings are almost identical (Fig. 5A), as evidenced by the similar α at the maximum C_L:C_D (Fig. 5B). The maximum C_L:C_D for wings in downstroke posture was 6.3, which occurred at α=26.5 deg. Wings in upstroke posture had a lower maximum C_L:C_D of 2.5, at α=28.0 deg. At measured *in vivo* α=66 deg during mid-upstroke, the C_L:C_D is approximately 0.91. At this α, C_L=1.33 and C_D=1.46. The C_L:C_D for downstroke posture was 3.33 at the *in vivo* α=46 deg, with C_L=1.54 and C_D=0.49.

Bracketing *in vivo* performance

Various assumptions provided alternative estimates for *in vivo* force production. We observed minimum values for lift and drag if we assumed a bird was hovering, with no forward translational velocity (Eqns 5 and 6). In this instance, the bird (4.37 N) would produce a resultant force ($\mathbf{F_R}$) of 51.3% body weight (2.24 N) with both wings during mid-downstroke (α=46 deg). During mid-upstroke (α=66 deg), the pigeon could produce a $\mathbf{F_R}$ of 107% body weight (4.71 N).

However, these values likely do not represent *in vivo* performance: during the third wingbeat following take-off, the bird has already reached a forward velocity of 2.9 m s^{-1}. When including this translation in our estimation by incorporating translational velocity (V_T) in a blade-element analysis (Eqn 8), mid-downstroke $\mathbf{F_R}$ produces 8.7 N, 198% of body weight. With a stroke plane angle of 38 deg during downstroke, the $\mathbf{F_R}$ is directed in front of the bird but near vertical, at 71 deg from the global horizontal plane, thus providing mostly weight support. During mid-upstroke, $\mathbf{F_R}$=5.43 N, 124% body weight. The upstroke stroke plane angle is 21 deg, and

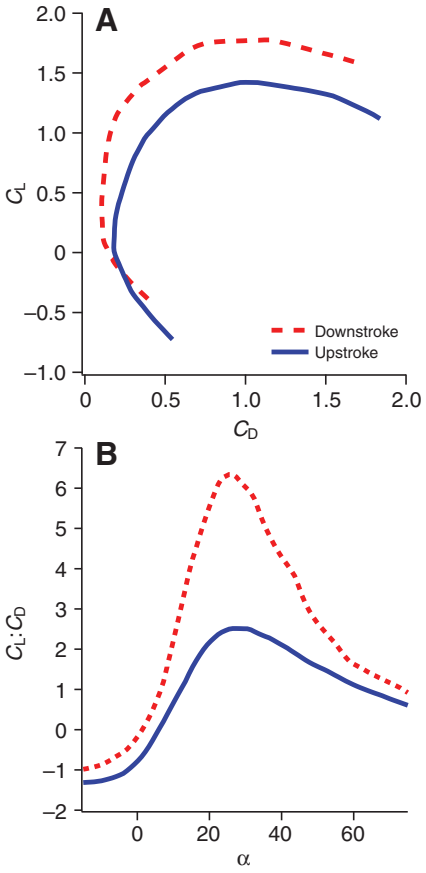

Fig. 5. (A) Polar diagram showing mean coefficient of lift (C_L) as a function of mean coefficient of drag (C_D) for *N*=3 pigeon wings. (B) Mean lift-to-drag ratio (C_L:C_D) against angle of attack (α) for *N*=3 pigeon wings.

$\mathbf{F_R}$ is oriented in front of the bird, 23 deg above the global horizontal plane, providing mostly thrust. These values probably represent extremes. Consider that mid-downstroke values appear to reflect the kinematics through the majority of downstroke (Fig. 3), while mid-upstroke kinematics reflects only a small portion of the entire half-cycle (Fig. 3). Extrapolating this calculation for the entire downstroke, which is approximately 58% of the wingbeat cycle, suggests that the bird produces a mean force of 115% body weight during downstroke. Throughout the entire upstroke, 42% of the wingbeat cycle, the mean force produced would be 36% bodyweight.

DISCUSSION

Given the debate over the functional significance of the tip-reversal upstroke (Brown, 1963; Spedding et al., 1984; Spedding, 1986; Aldridge, 1987; Hedrick et al., 2004; Tobalske et al., 2003), our most important result is that the model wings in upstroke posture produced a large amount of aerodynamic force (Figs 4 and 5). In fact, the downstroke and upstroke wings appear to perform similarly, both reaching maximum C_L:C_D at approximately α=26 deg (Fig. 5). This suggests that during mid-upstroke, significant force can be produced to help support weight or generate thrust, and the magnitude of this force is dependent on α in much the same way as for downstroke.

At *in vivo* angles of attack, we estimate the upstroke is capable of producing mean force as great as 36% body weight during this half of the stroke cycle. This value is within the range of lift produced

by an active upstroke in hovering hummingbirds (33–48%) (Warrick et al., 2005; Warrick et al., 2009). Our results are supported by measures of feather bending during slow flight. Values of strain on primary feathers during upstroke are 43% that of downstroke (Corning and Biewener, 1998), suggesting that upstroke values reported here are not unreasonable for *in vivo* performance. The upstroke force we estimated also falls near the range of 14% the lift of downstroke measured with accelerometers in cockatiels (Hedrick et al., 2004).

Aerodynamically active upstrokes have been reported in several bat species that exhibit a similar wing-tip reversal pattern. The horseshoe bat (*Rhionolophus ferrumenquinum*) has an angle of incidence at the wingtip during upstroke of 70 deg (Aldridge, 1986), close to our reported value of 66 deg. Introductory analyses of changes in acceleration found an aerodynamically active upstroke during vertical flight (Aldridge, 1987) and hovering (Aldridge, 1991) of bats. In-depth kinematic analyses accounting for inertial effects will be crucial to validate these findings. More recent analyses of the wake in slow-flying bats using PIV show a vortex ring shed at the end of upstroke (Hedenström et al., 2007; Johannson et al., 2008), indicating both thrust and weight support produced on the upstroke. Further PIV analyses show that the role of upstroke changes to only provide weight support at higher speeds in bats (Wolf et al., 2010). Our results suggest that birds exhibiting tip-reversal upstroke may use aerodynamic mechanisms similar to bats during slow flight.

Our findings indicate that slow-flying pigeons are using their wings at a lower C_L:C_D than is potentially available to them (Fig. 5A) during both upstroke and downstroke. However, they are operating at α close to, or at, maximum lift performance (Fig. 5B). Peak C_L for downstroke was 1.8 at α=61 deg, and for upstroke it was 1.4 at α=54 deg. At such high α on the upstroke, pigeons appear to be operating where lift and drag are almost equivalent (C_L:C_D=0.91). The resultant force during mid-upstroke is directed forward, 23 deg from global horizontal, due in part to high drag. This suggests that drag may play an important role during the upstroke, possibly to assist in weight support or thrust. This may also be the case for bats in slow flight (Aldridge, 1987; Norberg, 1976), and for chukar partridges during wing-assisted incline running (Tobalske and Dial, 2007).

Our propeller measurements for downstroke were consistent with previously published values for a pigeon wing in downstroke posture. Usherwood reports a maximum C_L:C_D of 5.4 for a pigeon wing spun on a propeller emulating slow flight (Usherwood, 2009), in comparison to our C_L:C_D of 6.3 (Fig. 5B). Maximum C_L for the same wings was 1.64 (Usherwood, 2009), while our value was 1.77. Our slightly higher values are potentially due to differences in wing morphology (Table 1) and spinning speed. Estimated lift and drag values for downstroke from kinematic analyses of pigeons in slow flight (Berg and Biewener, 2008) yielded values of C_L=1.44±0.29 and C_D=1.01±0.08, within the bounds of our values. Notably, the s.d. variation for C_L and C_D between wings increases with higher α in downstroke wings, but equivalent variation did not occur for upstroke wings. During slow flight, unsteady aerodynamic effects likely dominate (Ellington, 1984). At such high α, this may include periodic leading edge vorticity (Warrick et al., 2005) detachment. This flow separation may lead to unpredictable variation in both C_L and C_D throughout the half-stroke. In contrast, wings in upstroke posture, with smaller observed s.d. at high angles of attack, may reduce these effects *via* the separation of the primary feathers, allowing individual feathers to function as individual airfoils with lower α (Brown, 1963). Further exploration using flow-visualization would help tease apart differences between *in vivo* and propeller aerodynamics.

It is important to note that values reported here represent values for mid-stroke. Our estimate of *in vivo* $\mathbf{F_R}$ provide a lower bracket for downstroke of 51% bodyweight during hovering, and an upper bracket of 198% when accounting for translation (V_T). The resultants from these calculations are directed up 71 deg from global horizontal, indicating the downstroke acts to support weight. The same calculation for upstroke suggests a bracket between 107 and 124% body weight. The upstroke resultant is directed forward, 23 deg from global horizontal due to high levels of drag, suggesting upstroke provides thrust. These values likely provide a reasonable estimate for downstroke. Even then, wing velocity is greatest at mid-stroke, when our estimates are based, and resulting forces should be proportional to the square of wing velocity (Ellington, 1984). The values for upstroke are likely an over-estimate, as we applied static coefficients to a highly unsteady event. In the upstroke, α and wing velocity are highly time variant (Fig. 3), and our estimation occurred at near peak wing velocity. Moreover, wing posture appears to change more dramatically throughout the upstroke when compared with the downstroke, and it may be the mid-stroke posture that is optimal for force production. Our kinematic analysis throughout the stroke cycle (Fig. 3) illustrates that as the hand wing pronates using a rapid 'flick' at the end of upstroke, a changing α occurs, as also observed to a lesser extent in the downstroke in the pigeon (Warrick and Dial, 1998) and cockatiel (Hedrick et al., 2002). Such constant variation in wing velocity and α in upstroke is also exhibited by hovering hummingbirds, and it appears that this helps to explain variation in circulation on the wing (Tobalske et al., 2007; Warrick et al., 2009). Thus, our final estimate for net force produced during both halves of the stroke cycle, using Ω_r and accounting for the percentage of the total wingbeat cycle, is probably the most accurate for predicting pigeon performance.

Additionally, it is critical to note that the dried wing models do not accurately reflect all aspects of mid-downstroke or mid-upstroke. The preparation process, in which wings are isolated and dried, likely changes the mechanical properties of the wing. Similarly, the posture adopted by the models may not be an accurate representation of actual kinematics, as evidenced in slight differences in feather location between pigeon and propeller measurements (Fig. 2). While our model reflects the forces during an impulse, in reality the wing is morphing throughout most of the stroke cycle. For example, wing flexibility and compliance throughout a stroke significantly increases lift in insects (Mountcastle and Daniel, 2009; Young et al., 2009). During the stroke cycle of the pigeon, significant pronation and supination also occur. This results in wing camber and wing twist, which significantly improve aerodynamic forces in the locust (Young et al., 2009). The propeller model wings are probably unable to fully reflect these characteristics.

Our measure of α on the propeller is the geometric angle of attack, which does not account for induced velocity. It is likely that the angle of incidence (Vogel, 1994) was lower than our reported α. While our calculations of C_L and C_D account for local induced velocity (ε, Eqns 3 and 4), note that α is reported without accounting for local induced velocity. Thus, for example, a calculation for our mid-upstroke propeller model using a Rankine–Froude momentum jet model (Usherwood and Ellington, 2002a; Vogel, 1994) suggests that local induced velocity at the wingtip would be ~1.26 m s^{-1}. Therefore, the angle of incidence would be 52 deg, compared with 65 deg for α. To explore the possible impact of induced velocity throughout the stroke cycle, we present a simulated α throughout the stroke cycle (Fig. 3A, dotted line). This rough calculation using the same momentum jet model accounts for induced velocity during the downstroke, assuming that the induced velocity of the

downstroke heavily influences the upstroke as it returns through the downstroke wake. In general, these effects appear minimal (~10 deg), but have most pronounced effects at the downstroke–upstroke transition. Empirical measures of induced velocity would improve understanding of wing function *in vivo*, but will require methods such as PIV (Spedding and Hedenström, 2009) or hot-wire anemometry (Norberg et al., 1993).

CONCLUSIONS

The propeller, while a simplification of the wingbeat, provides new insight into the functional significance of the tip-reversal upstroke in avian flight. It has often been assumed that the tip-reversal posture in birds is simply to reduce drag by allowing air to pass through individual feathers, creating a Venetian blind effect (Brown, 1953; Brown, 1963). Thus far, hummingbirds are the only birds that are known to use an aerodynamically active upstroke during slow flight (Warrick et al., 2005). Our new measurements indicated that tip-reversal upstroke, widespread in birds with pointed wings, might be more similar to the hummingbird wingbeat than previously thought. If an aerodynamically active upstroke does offer advantages, why is it that not all birds use a tip-reversal? A future challenge will be to better understand the trade-offs that have led to many species with rounded wings using a flexed-wing upstroke.

LIST OF SYMBOLS

c	chord length
C_D	coefficient of drag
C_h	mean horizontal force coefficient
C_L	coefficient of lift
C_v	mean vertical force coefficient
$\mathbf{D}$	drag
$\mathbf{F_h}$	horizontal force
$\mathbf{F_R}$	resultant force
$\mathbf{F_v}$	vertical force
$\mathbf{L}$	lift
Q	torque about the motor
r	radial distance along the wing
R	wing length
S	wing area
S_2	second moment of area
S_3	third moment of area
V_T	wing translational velocity
α	geometric angle of attack
ε	downwash angle
ρ	air density
Ω	angular velocity

ACKNOWLEDGEMENTS

We thank Ashley Heers and Terry Dial for help with the development our propeller model and methods of data analysis. We thank Brandon Jackson, Ashley Heers, Ken Dial and two anonymous reviewers for helpful comments on a draft of this manuscript. Supported by NSF grants IOS-0923606 and IOS-0919799.

REFERENCES

Aldridge, H. D. J. N. (1986). Kinematics and aerodynamics of the greater horseshoe bat, *Rhionolophus ferrumenquinum*, in horizontal flight at various flight speeds. *J. Exp. Biol.* **126**, 479-497.
Aldridge, H. D. J. N. (1987). Body accelerations during the wingbeat in six bat species: the function of the upstroke in thrust generation, *J. Exp. Biol.* **130**, 275-293.
Aldridge, H. D. J. N. (1991). Vertical flight in the greater horseshoe bat *Rhinolophus ferrumequinum*. *J. Exp. Biol.* **157**, 183-204.
Altshuler, D. L., Dudley, R. and Ellington, C. P. (2004). Aerodynamic forces of revolving hummingbird wings and wing models. *J. Zool. Lond.* **264**, 327-332.
Berg, A. M. and Biewener, A. A. (2008). Kinematics and power requirements of ascending and descending flight in the pigeon (*Columba livia*) *J. Exp. Biol.* **211**, 1120-1130.
Brown, R. H. J. (1953). The flight of birds. II. Wing function in relation to flight speed. *J. Exp. Biol.* **30**, 90-103.
Brown, R. H. J. (1963). The flight of birds. *Biol. Rev. Camb. Philos.* **38**, 460-489.
Corning, W. R. and Biewener, A. A. (1998). *In vivo* strains in pigeon flight feather shafts: implications for structural design. *J. Exp. Biol.* **201**, 3057-3066.
Dickinson, W. B. and Dickinson, M. H. (2004). The effect of advance ratio on the aerodynamics of revolving wings. *J. Exp. Biol.* **207**, 4269-4281.
Ellington, C. P. (1984). The aerodynamics of hovering insect flight. VI. Lift and power requirements. *Philos. Trans. R. Soc. B* **305**, 145-181.
Ellington, C. P. (1991). Limitations on animal flight performance. *J. Exp. Biol.* **160**, 71-91.
Hedenström, A., Johansson, L. C., Wolf, M., von Busse, R., Winter, Y. and Spedding, G. R. (2007). Bat flight generates complex aerodynamic tracks. *Science* **316**, 894-897.
Hedrick, T. L. (2008). Software techniques for two- and three-dimensional kinematic measurements of biological and biomimetic systems. *Bioinspir. Biomim.* **3**, 034001.
Hedrick, T. L., Tobalske, B. W. and Biewener, A. A. (2002). Estimates of circulation and gait change based on a three-dimensional kinematic analysis of flight in cockatiels (*Nymphicus hollandicus*) and ringed turtle-doves (*Streptopelia risoria*). *J. Exp. Biol.* **205**, 1389-1409.
Hedrick, T. L., Usherwood, J. R. and Biewener, A. A. (2004). Wing inertia and whole-body acceleration: an analysis of instantaneous aerodynamic force production in cockatiels (*Nymphicus hollandicus*) flying across a range of speeds. *J. Exp. Biol.* **207**, 1689-1702.
Heers, A. M., Tobalske, B. W. and Dial, K. P. (2011). Ontogeny of lift and drag production in ground birds. *J. Exp. Biol.* **214**, 717-725.
Johansson, L. C., Wolf, M., vone Busse, R., Winter, Y., Spedding, G. R. and Hedenström, A. (2008). The near and far wake of Pallas' long tongued bat (*Glossophaga soricina*). *J. Exp. Biol.* **211**, 2909-2918.
Mountcastle, A. M. and Daniel, T. L. (2009). Aerodynamic and functional consequences of wing compliance. *Exp. Fluids* **46**, 873-882.
Norberg, U. M. (1976). Aerodynamics, kinematics, and energetics of horizontal flapping flight in long-eared bat (*Plecotus auritus*). *J. Exp. Biol.* **65**, 179-212.
Norberg, U. M., Kunz, T. H., Steffensen, J. F., Winter, Y. and Von Helversen, O. (1993). The cost of hovering and forward flight in a nectar-feeding bat, *Glossophaga soricina*, estimated from aerodynamic theory. *J. Exp. Biol.* **182**, 207-227.
Osborne, M. F. M. (1951). Aerodynamics of flapping flight with application to insects. *J. Exp. Biol.* **28**, 221-245.
Rayner, J. M. V. (1995). Flight mechanics and constraints on flight performance. *Israel J. Zool.* **41**, 321-342.
Spedding, G. R. (1986). The wake of a jackdaw (*Corvus monedula*) in slow flight. *J. Exp. Biol.* **125**, 287-307.
Spedding, G. R. and Hedenström, A. (2009). PIV-based investigations of animal flight. *Exp. Fluids* **46**, 749-763.
Spedding, G. R., Rayner, J. M. V. and Pennycuick, C. J. (1984). Momentum and energy in the wake of a pigeon (*Columba livia*) in slow flight. *J. Exp. Biol.* **111**, 81-102.
Tobalske, B. W. (2000). Biomechanics and physiology of gait selection in flying birds. *Phys. Biochem. Zool.* **73**, 736-750.
Tobalske, B. W. and Dial, K. P. (1996). Flight kinematics of black-billed magpies and pigeons over a wide range of speeds. *J. Exp. Biol.* **199**, 263-280.
Tobalske, B. W. and Dial, K. P. (2000). Effects of body size on take-off flight performance in the *Phasianidae* (*Aves*). *J. Exp. Biol.* **203**, 3319-3332.
Tobalske, B. W. and Dial, K. P. (2007). Aerodynamics of wing-assisted incline running in birds. *J. Exp. Biol.* **210**, 1742-1751.
Tobalske, B. W., Hedrick, T. L. and Biewener, A. A. (2003). Wing kinematics of avian flight across speeds. *J. Avian Biol.* **34**, 177-184.
Tobalske, B. W., Warrick, D. R., Clark, C. J., Powers, D. R., Hedrick, T. L., Hyder, G. A. and Biewener, A. A. (2007). Three-dimensional kinematics of hummingbird flight. *J. Exp. Biol.* **210**, 2368-2382.
Usherwood, J. R. (2009). The aerodynamic forces and pressure distribution of a revolving pigeon wing. *Exp. Fluids* **46**, 991-1003.
Usherwood, J. R. and Ellington, C. P. (2002a). The aerodynamics of revolving wings – I. Model hawkmoth wings. *J. Exp. Biol.* **205**, 1547-1564.
Usherwood, J. R. and Ellington, C. P. (2002b). The aerodynamics of revolving wings – II. Propeller force coefficients from mayfly to quail. *J. Exp. Biol.* **205**, 1565-1576.
Usherwood, J. R., Hedrick, T. L., McGowan, C. P. and Biewener, A. A. (2005). Dynamic pressure maps for wings and tails of pigeons in slow, flapping flight, and their energetic implications. *J. Exp. Biol.* **208**, 355-369.
Vogel, S. (1994). *Life in Moving Fluids: The Physical Biology of Flow.* Princeton: Princeton University Press.
Warrick, D. R. and Dial, K. P. (1998). Kinematic, aerodynamic, and anatomical mechanisms in the slow, maneuvering flight of pigeons. *J. Exp. Biol.* **201**, 655-672.
Warrick, D. R., Tobalske, B. W. and Powers, D. R. (2005). Aerodynamics of the hovering hummingbird. *Nature* **435**, 1094-1097.
Warrick, D. R., Tobalske, B. W. and Powers, D. R. (2009). Lift production in the hovering hummingbird. *Proc. R. Soc. B.* **276**, 3747-3752.
Weis-Fogh, T. (1973). Quick estimates of flight fitness in hovering animals, including novel mechanisms for lift production. *J. Exp. Biol.* **59**, 169-230.
Wolf, M., Johansson, L. C., von Busse, R., Winter, Y. and Hedenström, A. (2010). Kinematics of flight and the relationship to the vortex wake of the Pallas' long tongued bat (*Glossophaga soricina*). *J. Exp. Biol.* **213**, 2142-2153.
Young, J., Walker, S. M., Bomphrey, R. J., Taylor, G. K. and Thomas, A. L. R. (2009). Details of insect wing design and deformation enhance aerodynamic function and flight efficiency. *Science* **325**, 1549-1552.

© 2015. Published by The Company of Biologists Ltd | The Journal of Experimental Biology (2015) 218, 2518-2527 doi:10.1242/jeb.116228

RESEARCH ARTICLE

Kinematics and aerodynamics of avian upstrokes during slow flight

Kristen E. Crandell* and Bret W. Tobalske

ABSTRACT

Slow flight is extremely energetically costly per unit time, yet highly important for takeoff and survival. However, at slow speeds it is presently thought that most birds do not produce beneficial aerodynamic forces during the entire wingbeat: instead they fold or flex their wings during upstroke, prompting the long-standing prediction that the upstroke produces trivial forces. There is increasing evidence that the upstroke contributes to force production, but the aerodynamic and kinematic mechanisms remain unknown. Here, we examined the wingbeat cycle of two species: the diamond dove (*Geopelia cuneata*) and zebra finch (*Taeniopygia guttata*), which exhibit different upstroke styles – a wingtip-reversal and flexed-wing upstroke, respectively. We used a combination of particle image velocimetry and near-wake streamline measures alongside detailed 3D kinematics. We show that during the middle of the wingtip-reversal upstroke, the hand-wing has a high angular velocity (15.3±0.8 deg ms^{-1}) and translational speed (8.4±0.6 m s^{-1}). The flexed-wing upstroke, in contrast, has low wingtip speed during mid-upstroke. Instead, later in the stroke cycle, during the transition from upstroke to downstroke, it exhibits higher angular velocities (45.5±13.8 deg ms^{-1}) and translational speeds (11.0±1.9 m s^{-1}). Aerodynamically, the wingtip-reversal upstroke imparts momentum to the wake, with entrained air shed backward (visible as circulation of 14.4±0.09 m^2 s^{-1}). In contrast, the flexed-wing upstroke imparts minimal momentum. Clap and peel in the dove enhances the time course for circulation production on the wings, and provides new evidence of convergent evolution on time-varying aerodynamic mechanisms during flapping in insects and birds.

KEY WORDS: Lift, Thrust, Clap and peel, Take-off, Wingtip-reversal, Flexed-wing, Particle image velocimetry

INTRODUCTION

Takeoff, landing and slow flight are critical phases for all flying animals, whether foraging, evading predation or finding a mate. Slow flight (<3 m s^{-1}) is also an energetically costly form of flight (Tobalske et al., 2003). The aerodynamics of this important form of flight are not well understood because the majority of research on bird flight aerodynamics has focused either on hovering in hummingbirds (Warrick et al., 2005, 2009) or on medium- and high-speed flight (Spedding et al., 2003a,b; Spedding and Hedenstrom, 2009; Henningsson et al., 2011; Spedding and Hedenstrom, 2009). Here, we set out to test the hypothesis that there is aerodynamic activity during the general avian (i.e. non-hummingbird) upstroke, an idea proposed first by Marey (1890) and subsequently by Lorenz (1933) and Brown (1953). We describe the kinematic and aerodynamic patterns of slow flight in two species of birds, the diamond dove and the zebra finch, with two distinct upstroke styles: wingtip-reversal and flexed-wing upstroke.

When engaged in slow flight, birds generally do not maintain an extended wing. Instead, all birds except hummingbirds (Warrick et al., 2005) fold or flex their wings on the upstroke (Tobalske, 2007). During medium and fast flight in many species, the wing is kept partially extended during upstroke, and so is understood to be aerodynamically active (Spedding et al., 2003b), particularly at faster speeds (Henningsson et al., 2011). In contrast, the observed kinematic patterns during slow flight have prompted the well-established prediction that the upstroke is aerodynamically inactive, halving the amount of time during a wingbeat that a bird can produce useful forces. Few direct measures of the kinematics and aerodynamics of upstroke in slow flight exist, however (Chang et al., 2013; Hedenström et al., 2006; Lentink et al., 2015; Muijres et al., 2012a,b,c; Spedding et al., 2003a). Most studies of takeoff flight focus on the immediate transition from legs to wings (Berg and Biewener, 2010; Earls, 2000; Provini et al., 2012).

During slow flight, most birds have one of two upstroke patterns: a flexed-wing upstroke or a wingtip-reversal upstroke. During the flexed-wing upstroke, the entire wing is pulled toward the body. Birds with this pattern generally have low aspect ratio, rounded wing tips (Brown, 1963). A study of slow flight in flycatchers (*Ficedula hypoleuca*) found no evidence for an aerodynamically active flexed-wing upstroke (Muijres et al., 2012a). The flexed-wing upstroke becomes aerodynamically active gradually as flight speed increases from 4 m s^{-1} to 8 m s^{-1} in both the thrush nightingale (Spedding et al., 2003b) and the robin (Hedenström et al., 2006), yet aerodynamic activity at speeds less than 4 m s^{-1} remains untested. The contrasting wingtip-reversal upstroke style keeps the distal wing extended, with the primary feathers supinated but traveling through an arc in the air. Birds with pointed, high aspect-ratio wingtips tend to exhibit a tip-reversal upstroke during slow flight (Simpson, 1983; Tobalske, 2007); galliformes are an exception (Tobalske and Dial, 2000).

Several lines of evidence suggest the tip-reversal upstroke produces aerodynamic force. Feather loading in live pigeons (*Columba livia*) and propeller models using pigeon wings suggest that the tip-reversal upstroke is aerodynamically active (Corning and Biewener, 1998; Crandell and Tobalske, 2011). *In vivo* accelerometers mounted to the trunk of a cockatiel (*Nymphicus hollandicus*) also indicate that the tip-reversal upstroke produces 14% of the net force of downstroke (Hedrick et al., 2004). Lastly, kinematic analyses of pigeons suggest the upstroke produces 50% of the net force of the downstroke during slow-speed maneuvering (Ros et al., 2011). However, the aerodynamic mechanism remains unknown.

It has been hypothesized, based on wing kinematics (Bennett, 1977; Scholey, 1983; Simpson, 1983), that birds which produce a tip-reversal upstroke capitalize on a time-varying mechanism called clap and fling (or clap and peel). This mechanism creates circulation at the transition from upstroke to downstroke via an interaction

Field Research Station at Fort Missoula, Division of Biological Sciences, University of Montana, Missoula, MT 59812, USA.

*Author for correspondence (kristen.crandell@gmail.com)

Received 2 November 2014; Accepted 25 May 2015

The Journal of Experimental Biology

The Journal of Experimental Biology (2015) 218, 2518-2527 doi:10.1242/jeb.116228

List of symbols and abbreviations

A	area swept by the wing
c	wing chord
F	net force
PIV	particle image velocimetry
T	time interval
u	average airspeed
V_A	angular velocity
V_T	global wingtip speed
α	global angle of attack
β	angle between wings
Γ	circulation
ρ	air density
ω	vorticity

Table 1. Morphometrics for individual birds

	Mass (g)	Wing area (cm^2)	Wing length (cm)	Wing chord (cm)	Aspect ratio
Dove					
2	43.3	46.81	10.56	5.79	0.99
3	38.7	38.67	9.65	4.99	1.10
4	40.3	60.14	11.54	5.62	0.83
5	38.2	75.45	11.83	6.59	0.68
Mean±s.d.	40.1±2.3	55.3±16.1	10.9±1.0	5.7±0.6	0.9±0.2
Finch					
1	13	29.41	6.92	4.69	1.08
2	12.2	28.7	6.62	5.8	1.06
3	12.1	36.79	8.44	5.32	1.03
4	12.5	29.88	8.04	4.59	1.21
Mean±s.d.	12.5±0.4	7.5±0.9	5.1±0.6	5.1±0.6	1.1±0.1

All birds were used in particle image velocimetry (PIV) and kinematic analyses. Dove 4 and finch 1 were used in smoke-line flow studies.

between the left and right wings. Similar insect kinematic patterns were first observed in *Drosophila melanogaster* and described by Vogel (1967). Weis-Fogh described this pattern in the chalcid wasp *Encarsia formosa* and predicted this motion increases the strength of circulation around the wing (Weis-Fogh, 1973). Subsequent models indicated the fling is aerodynamically active (Maxworthy, 1979) by initiating circulation immediately along the wing. This circulation contributes heavily to a leading-edge vortex that grows throughout the downstroke (Sane, 2003). Clap and fling is observed in a large insect, the hawkmoth (*Re*=8000) (Bomphrey et al., 2006). Theory and empirical measurements with flapper models both indicate a boost in force production via this mechanism (Ellington, 1984; Lehmann et al., 2005). Among birds, there exists aerodynamic evidence that Japanese white-eye (*Zosterops japonicus*) and Gouldian finch (*Erythrura gouldiae*) capitalize on a ventral clap, wherein the wings are brought together beneath the body to contribute to the downwash (Chang et al., 2013). Here, we differentiate between a clap and fling versus a clap and peel, as defined by Miller and Peskin (2009): we define a clap and fling as minimal flexibility in a rigid wing structure, wherein changes in shape are from external mechanisms, such as aerodynamic loading and inertia; clap and peel, then, has flexibility spanwise and chordwise along the wing, and shape changes are both passive and active via musculoskeletal control.

We undertook the present study to test for aerodynamic activity in both upstroke styles, and describe the kinematics in relation to the forces they produce. We tested the following hypotheses: the kinematic clap and peel pattern yields flow regimes similar to the clap and peel of insect flight, despite dramatic differences in body size and, thus, Reynolds number (hawkmoth *Re*=8000, dove *Re*=51,000). Additionally, the flexed-wing upstroke will be aerodynamically inactive. In both birds, we additionally expected the aerodynamic circulation (or lack thereof) produced during the upstroke would carry over and impact the circulation produced during the downstroke. To address these hypotheses, we compared two species: the diamond dove [*Geopelia cuneata* (Latham 1801), 40 g], which exhibits a wingtip-reversal upstroke, and the zebra finch (*Taeniopygia guttata* Reichenbach 1862, 13 g), which uses a flexed-wing upstroke.

RESULTS

Kinematics

We analyzed kinematic patterns for the third wingbeat in a flight sequence for four birds of both species (morphometrics available in Table 1). All flights were within ±5 deg of level flight. In kinematic trials, the doves had an average body velocity of 1.54±0.36 m s^{-1}, while the finches had an average body velocity of 1.03±0.28 m s^{-1}. During the third wingbeat, the doves were still accelerating at an average of 5.5±0.54 m s^{-2}, and finches were accelerating at 4.34±1.54 m s^{-2}.

Three-dimensional traces of the path of the wingtips of the dove and finch followed the general pattern of the lateral-view kinematics of the rock pigeon and black-billed magpie (*Pica hudsonia*), respectively, as described in Tobalske and Dial (1996). Our 3D analysis revealed a figure-of-eight pattern in the dorsal and sagittal plane of the dove, but not in the finch (Fig. 1). The finch pattern produced a near-complete semi-circle in both the dorsal and sagittal planes, where the wingtip (black line) was kept caudal to the body during the upstroke, and oriented cranially during downstroke. In the dove, the wingtip transitioned from cranial to caudal during the upstroke (Fig. 1, dorsal and sagittal planes). A further difference between the species was visible in the transverse plane. In the dove, the hand-wing was kept extended (80.2±3.2% of wing length) during both upstroke and downstroke. In contrast, the finch flexed the wing (64.8±5.2% of wing length) during upstroke, most noticeably in the wrist kinematics (Fig. 1, transverse plane).

The global angle of attack (α, defined as the angle between the velocity vector of the hand-wing and the wrist–secondary feather chord line) differed between species during upstroke, but followed a similar trend (Fig. 2A). The dove had a negative α during upstroke, with a minimum of −81.3±4 deg during the first third of upstroke. The dove transitioned from a negative to a positive α at wing turn around. In the finch, during upstroke, α remained negative, with a minimum value of −45.9±7.3 deg. As the transition between upstroke and downstroke approached, α transitioned through 0 deg, peaking during the downstroke at 51.5±7.4 deg.

Global wingtip speed (V_T) showed similar patterns between the dove and finch (Fig. 2B). In the dove, there were two peaks in V_T, the first during upstroke at 8.4±0.6 m s^{-1}, and the second during downstroke at 9.9±1.3 m s^{-1}. These indicate maximal V_T produced during the middle of the limb swing phase, at the transition from limb acceleration to limb deceleration. The finch also exhibited two peaks, although the peak during upstroke remained for approximately 5 ms. During the upstroke, peak V_T was 7.5±3.3 m s^{-1}. During the downstroke, V_T peaked at 11.0±1.9 m s^{-1}. This peak occurred following the transition from upstroke to downstroke, and so took place relatively earlier in the finch than the dove.

Angular velocities (V_A) were defined as the angular change between the orientation of the position vector of the hand-wing

The Journal of Experimental Biology (2015) 218, 2518-2527 doi:10.1242/jeb.116228

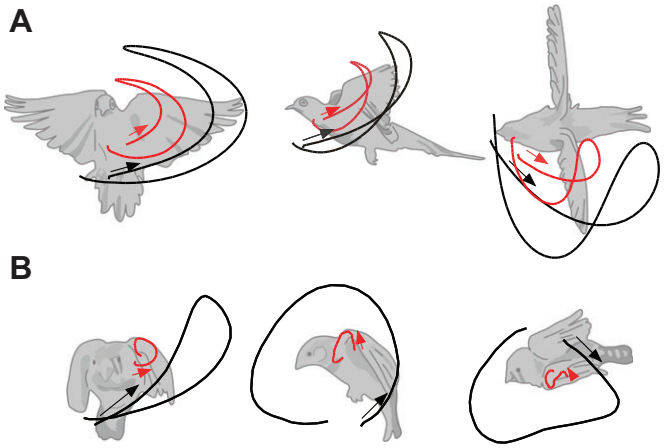

Fig. 1. Traces of representative bird-centered wingtip and wrist movements of the study species. (A) Diamond dove, (B) zebra finch. Traces (left to right) are from the transverse, sagittal and dorsal planes (bird silhouettes represent the mid-upstroke position, and are not an exact representation of posture at that point in time). Wrists are represented in red, wingtips in black. Arrows indicate the start of upstroke (transition from downstroke, time 0%).

centroid points, in global coordinates. These velocities followed a similar pattern to wingtip speed in the dove, but not the finch (Fig. 2C). In the dove, two peaks in V_A occurred, in the same pattern as V_T – peaking halfway through upstroke at 15.3±0.8 deg ms^{-1} and halfway through downstroke at 19.4±2.1 deg ms^{-1}. In the finch, however, only one prominent peak in V_A occurred, at 45.4± 13.8 deg ms^{-1}, at the transition between upstroke and downstroke. At this point, the wing rapidly reoriented from being strongly adducted to being fully extended. A minor V_A peak occurred during the upstroke at 32.2±9.7 deg ms^{-1}, but this peak remained relatively stable until the transition between upstroke and downstroke.

Our analysis of wing–wing interactions in three dimensions illustrates each portion of the clap and peel cycle in the dove, relative to wing contact time (Fig. 3). In the wingtip-reversal at the end of the upstroke, the rapidly extending wings came into contact (the 'clap'), with the left and right wing leading edges coming together approximately 3 ms before the trailing edge, at approximately 5% of the entire wingbeat cycle. The wingtip leading edges were 1.5±0.6 cm apart (approximately the width between the shoulders) at closest contact, while the trailing edges reached almost full contact at 0.2±0.1 cm apart. Fig. 3A illustrates the leading edge (red, orange) on the right and left wing coming into contact (red arrow). The trailing edge (Fig. 3A, blue, green) came together later (blue arrow). Following the clap, the wings moved apart during the peel phase as downstroke began. The wings first separated at the leading edge (Fig. 3A, red arrow), with the trailing edge separation occurring 4–9 ms later (blue and green arrows).

In contrast, during the flexed-wing upstroke of the zebra finch, all points along the wing stayed close to the body during upstroke, with the wingtip at 3.2±0.4 cm between the left and right wings (approximately the width of the body, Fig. 3B). At the transition from upstroke to downstroke, the wings opened approximately 6.2±0.7 cm apart. Notably, the trailing edges of the finch did come close to contact during the transition from upstroke to downstroke (Fig. 3B, blue and green).

Aerodynamics

We analyzed the wake of four birds for each species (morphometrics available in Table 1). Zebra finches averaged a body velocity of

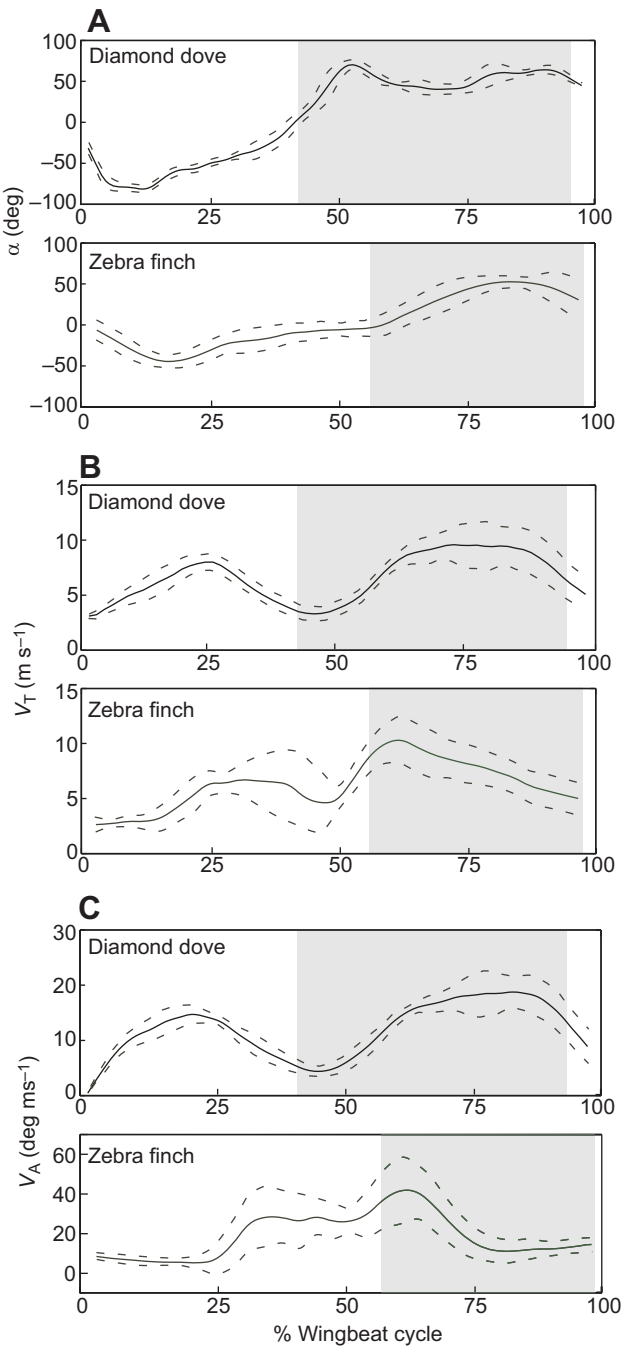

Fig. 2. Kinematic variables for the centroid of the hand-wing. (A) Angle of attack (α), (B) translational speed (wingtip speed, V_T) and (C) angular velocity (V_A). Data were extracted from the diamond dove and zebra finch during the third wingbeat of the downstroke. Solid lines represent means, dashed lines the standard deviations. The shaded area represents the downstroke.

1.03±0.28 m s^{-1} and diamond doves averaged a body velocity of 1.54±0.36 m s^{-1}; both species were accelerating. Flights analyzed with smoke visualization maintained free-stream velocities of approximately 0.95±0.05 m s^{-1}. All flights analyzed were within ±5 deg of level flight. We observed significant aerodynamic activity in the wingtip-reversal upstroke of the diamond dove, and minimal activity during the flexed-wing upstroke of the zebra finch. In the dove, a shed vortex was evident in our particle image velocimetry (PIV) images (Fig. 4) at the transition from upstroke to downstroke (circulation Γ=14.4±0.09 m s^{-2}). This same type of

The Journal of Experimental Biology (2015) 218, 2518-2527 doi:10.1242/jeb.116228

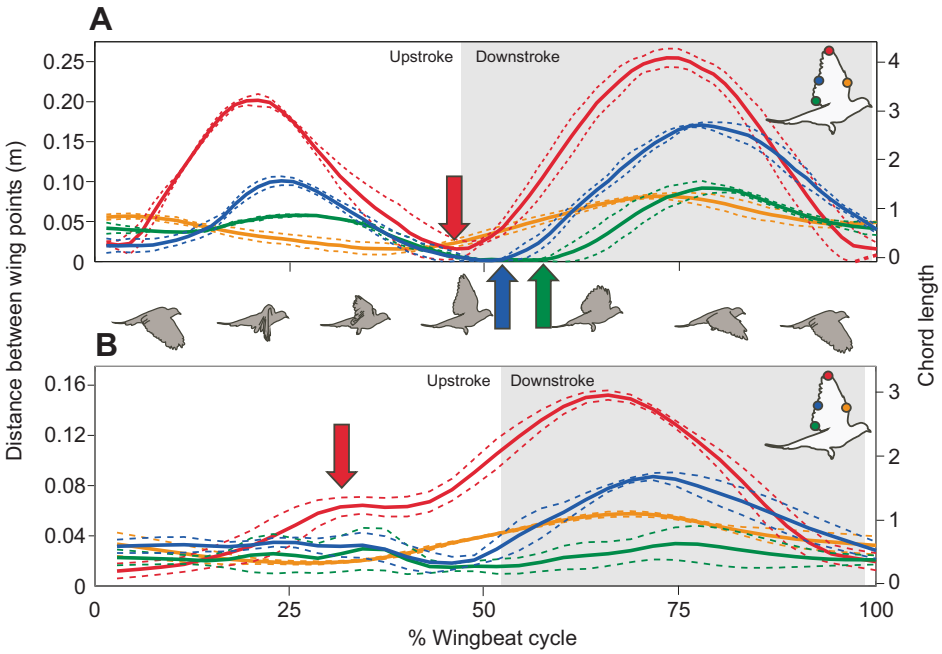

Fig. 3. Distances between opposite wings during the third full wingbeat cycle in diamond doves and zebra finches. (A) Distance between wing points in the diamond dove. Note the significant lag time between leading edge separation (red, orange) and trailing edge separation (blue, green). Arrows show contact and separation of wingtips (red) before trailing edges (blue, green). (B) Distance between wing points in the zebra finch. Note the distinct kinematic differences from the dove during upstroke, as the finch holds its wings close to the body during this phase (orange, blue, green). The leading edge wingtip (red) is held close to the body during the start of upstroke in the finch, and these edges begin to separate over 2/3 of the way through the upstroke time (red arrow). Means and s.e. are represented by solid and dashed lines, respectively. The scale on the right is relative to the wing chord (Table 1). Bird outlines between graphs are modeled after the diamond dove.

upstroke-generated vortex was never observed in PIV images from the zebra finch (Fig. 5).

During the last half of upstroke, the diamond dove hand-wing was aerodynamically active in that it displaced streamlines (Fig. 6A). Induced velocity to the air was visible as an abrupt cut-off between the smoke lines through which the wing moved, visible at 35% and 45% of the wingbeat cycle in Fig. 6A (red arrowhead and ellipse). At the end of upstroke (Fig. 6A, 55%), the wings came into contact, and the entrained air around the wings was shed. As described above, we detected this shed vortex in our parasagittal samples of PIV images as circulation deposited into the wake at the transition between upstroke and downstroke in the diamond dove (Fig. 4A). Induced velocity behind the wing was also visible, at 2.73±0.23 ms^{-1} for an arbitrarily selected patch immediately behind the wings (Fig. 7).

From smoke lines near the finch, it was evident that the feathers act similar to those in the doves, imparting momentum to the wake; smoke was entrained on the primary feathers during upstroke (Fig. 6B, 10 ms, red arrowhead; supplementary material Movie 1). However, the surface area of the wing was much reduced in comparison to the dove (Fig. 6).

Both species created a starting vortex during the first part of downstroke (Fig. 4B and Fig. 5B), but the initiation of circulation appeared to be relatively earlier in the dove (Fig. 4A), which we interpret as being due to the clap and peel pattern of the wings, approximately concurrent with the shedding of circulation into the wake. We first measured this circulation in a parasagittal plane over the back of the bird as 26±3% the value of the final downstroke circulation (Fig. 8). In the dove, this circulation grew throughout the downstroke (Fig. 4), and reached values that were not significantly different from the final shed vortex halfway through the downstroke. In contrast, circulation measured in the zebra finch in the same plane was approximately 0% of final circulation values at the start of early downstroke (Fig. 5A and Fig. 8). This was a consequence of the lack of an initial shed vortex created during upstroke. However, as observed in the smoke line video, the finch had a start vortex that began independently on both wings, just like the dove (supplementary material Movie 1). As a consequence of this right and left wing-independent vortex ring structure (Pournazeri et al., 2013), the measured circulation in the sagittal plane dorsal to the bird was 20–40% lower in the finch at the start of downstroke, suggesting a relatively smaller time interval over which circulation was created. This smaller time frame was a consequence of the wings of the finch beginning the downstroke farther from the midline of the bird (Fig. 3).

Force estimates in the dove

To provide a rough estimate of the net forces that the clap and peel mechanism may provide relative to the subsequent downstroke, we adopted two models: a momentum-jet model (Vogel, 1994) focusing on downstroke, and a reverse peel model (Miller and Peskin, 2009), focusing on the clap. Both models assume steady-state flow conditions and circulation averages are representative of the wingbeat. As such, they are simplifications, and caution is necessary in interpreting the results; our goal was to provide initial quantitative estimates to help motivate future research that may employ time-resolved and volumetric techniques for flow measurement (e.g. Hubel et al., 2010; Bomphrey et al., 2012).

We estimate average force produced during the downstroke phase to be 0.74 N – 188% body weight for the average dove weight of 0.39 N. This is consistent with body weight estimates for the downstroke in a dove during steady flight on a level path given that downstroke is 60% of the total wingbeat cycle (Provini et al., 2012).

For the contribution of the clap in the reverse peel model, we incorporated the angle between the wings (50 deg) and induced velocity (2.5 m s^{-1}; Fig. 7). With these values, the reverse peel model indicates the clap phase may produce 0.35 N, or 89% of body weight. The reverse peel model does not include an estimate of force production during the translational phase of the upstroke, and so is likely an underestimate. We estimate the time duration for this average force production to be approximately 10 ms, or 15% of the total wingbeat cycle. In other words, the impulse from downstroke is approximately 0.031 N, while the impulse from upstroke is 0.0035 N.

DISCUSSION

In the two bird species we studied, we observed two distinct aerodynamic patterns, consistent with distinct wing kinematics.

The Journal of Experimental Biology (2015) 218, 2518-2527 doi:10.1242/jeb.116228

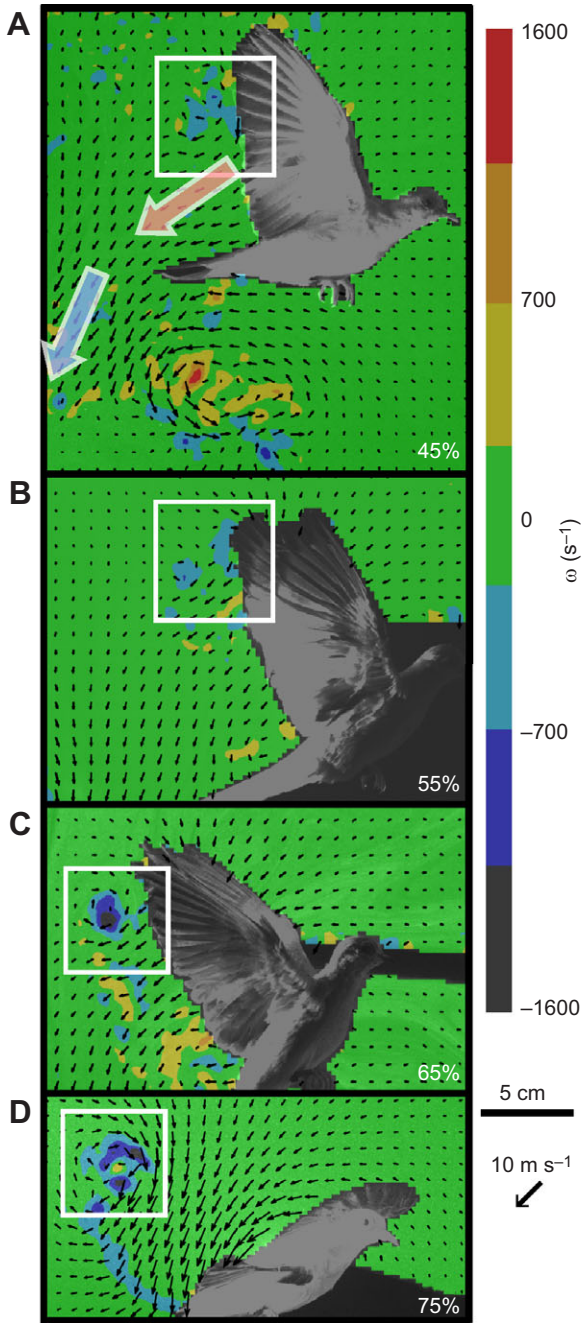

Fig. 4. A sequence of wake visualizations for the diamond dove clap and peel stroke cycle transition. The sequence was assembled using data from two individuals. Vectors in the foreground represent air velocity (m s^{-1}) and colors in the background indicate vorticity (ω, s^{-1}). White boxes indicate the vortex shed during the clap (A) and the downstroke vortex growing during the subsequent peel (B,C) and downstroke (D). Large arrows in A summarize the direction of airflow (blue, downwash from a previous downstroke; red, velocities imparted by the upstroke). The approximate percentage of the wingbeat cycle from kinematics in Figs 2 and 3 is indicated.

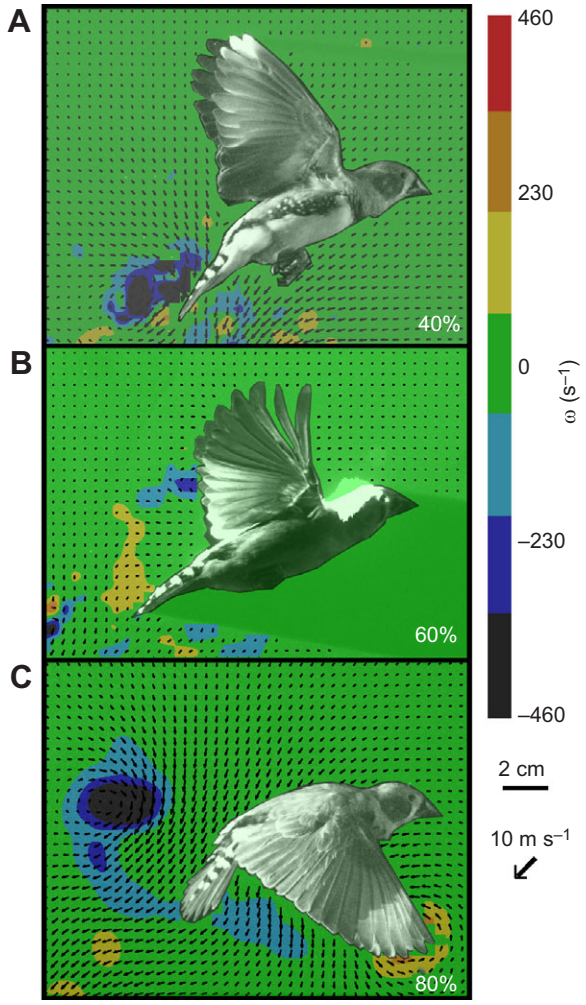

Fig. 5. A sequence of wake visualizations for the zebra finch upstroke to downstroke transition. The sequence was assembled using data from one individual. Vectors in the foreground represent air velocity (m s^{-1}) and colors in the background indicate vorticity (ω, s^{-1}). Note a lack of vorticity at the transition from upstroke to downstroke (A), and a lack of initiation of circulation during the first quarter of downstroke (B), until final levels are reached at the end of downstroke (C). The approximate percentage of the wingbeat cycle from kinematics in Figs 2 and 3 is indicated.

One, the wingtip-reversal upstroke in the dove, produces measurable circulation, evident as a vortex core and induced velocity approximately concurrent with the animal clapping and peeling its wings apart (Figs 4, 7). In contrast, some aerodynamic activity was apparent in streamlines during the flexed-wing upstroke of the zebra finch (Fig. 6B), but this activity was so minimal as to not be manifest in our parasagittal PIV images of the wake from this species (Fig. 5). We found support for our initial hypothesis that the clap and fling style kinematic pattern produces potentially useful aerodynamic forces (estimated at an average of 89% body weight produced during the clap). Further, we found that this capacity to generate aerodynamic force in late upstroke then continues uninterrupted throughout the subsequent downstroke. We found support for our second hypothesis in that the flexed-wing upstroke of the finch produces negligible aerodynamic forces, and as a consequence leads to relatively delayed growth in circulation during the downstroke.

We present α and V_T data for the finch (Fig. 2), but the negligible aerodynamic forces observed suggest that these measures may be irrelevant during the majority of the upstroke, particularly as the wing is kept near the body and so is likely not extended enough to induce momentum to the wake. Although evidence was lacking in our lateral PIV measures, the finch downstroke may be aerodynamically representing a distant-peel condition, wherein the left and right wing do not directly contact, but may be close enough to manifest an aerodynamic benefit similar to the peel

The Journal of Experimental Biology (2015) 218, 2518-2527 doi:10.1242/jeb.116228

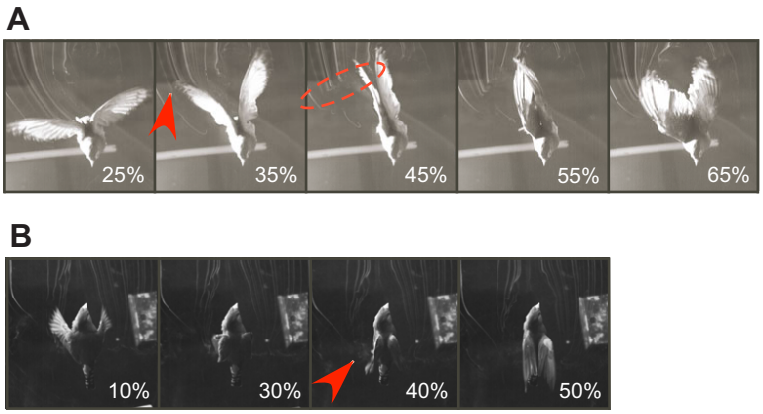

Fig. 6. Smoke-line traces of airflow during flight. (A) In the diamond dove, induced velocity is evident mid-way through the upstroke as a deflection of smoke lines (arrowhead) at 35%, and the disrupted wake visible at 45% (ellipse). (B) In the zebra finch, minimal aerodynamic activity is seen during the upstroke. A small amount of aerodynamic activity is visible at 40% (arrowhead). Approximate percentages of the wingbeat cycle are noted in conjunction with previous figures.

condition (Scholey, 1983). In particular, the peak wingtip velocity in the finch occurs during this phase, and may in fact contribute to the initial creation of circulation. Two passerine species demonstrate clap kinematics at the transition from downstroke to upstroke (Chang et al., 2013), so it is feasible that a similar pattern occurs during the upstroke to downstroke transition. Further work with high-speed, stereo PIV is necessary to explore this hypothesis. Wing inertia may play a crucial role in wing–wing contact (Hedrick et al., 2004); this may serve as an explanation for why short, rounded wing species use a flexed-wing upstroke, and long, pointed wing species typically use a wingtip-reversal upstroke (with the notable exception of the galliformes; Tobalske and Dial, 2000).

The kinematic patterns of the clap and peel during the transition from upstroke to downstroke appear different between insects and birds, likely because of different musculoskeletal arrangements. Birds actively pronate the leading edge of the wing to begin the peel phase, with the trailing edge following. Muscles in the distal wing are active during this phase (Dial, 1992), suggesting muscular control of the distal wing. Insects, however, do not have controlling muscles in their wings, and must rely on forces from indirect muscles deforming the trunk or direct muscles acting at the wing base to separate the two wings (Dudley, 2000). This morphological dissimilarity presents a difference in kinematics. For example, in *E. formosa* during transition from upstroke to downstroke, the clap phase alone constitutes between 20% and 25% of the entire wingbeat cycle (Ellington, 1975). In the dove, this phase is only 2% of the total wingbeat cycle. Further, unlike in theoretical models (Ellington, 1984), the vorticity produced by the clap phase in the dove appeared to be a direct result of shedding circulation created during the upstroke. This is visible in Fig. 6 at 25–45%, and the wake left behind is seen in Fig. 4. In insects, the clap phase expels air from between the left and right wing, similar to a jet (Miller and Peskin, 2009). However, in the dove, circulation created during the upstroke is shed during the clap phase.

The functional contribution of tip-reversal in slow forward flight appears to be as thrust rather than weight support. As the wings are moving caudally, induced velocity in the wake is convected caudally and laterally (supplementary material Movies 2,3). The observed shed vortex is oriented behind the bird, evident in the PIV image (Fig. 4A, red arrow). Shedding of vorticity was likely assisted by the rapid motion of the two wings coming into contact dorsally (Fig. 3, red arrow). In sum, these wing motions and the resulting induction of velocity into the air would likely be beneficial to a bird seeking to move forward. This observation is corroborated by our

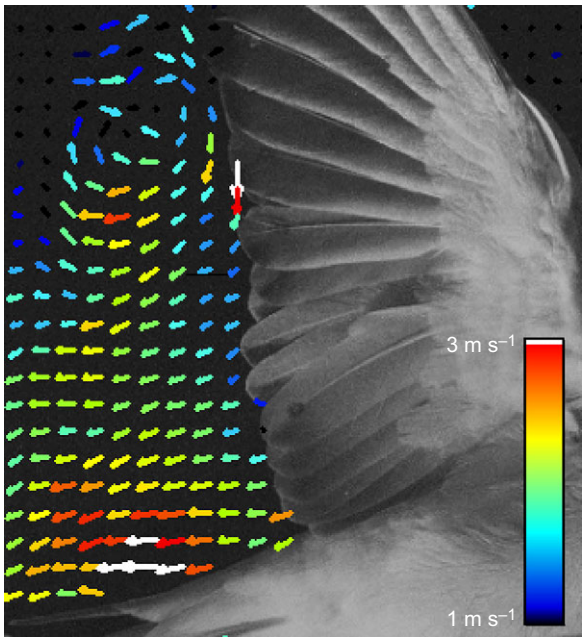

Fig. 7. Induced velocities behind the wing of the diamond dove, caused by motion during upstroke. Velocities behind the wing were created during the upstroke. The scale represents 1–3 m s^{-1}.

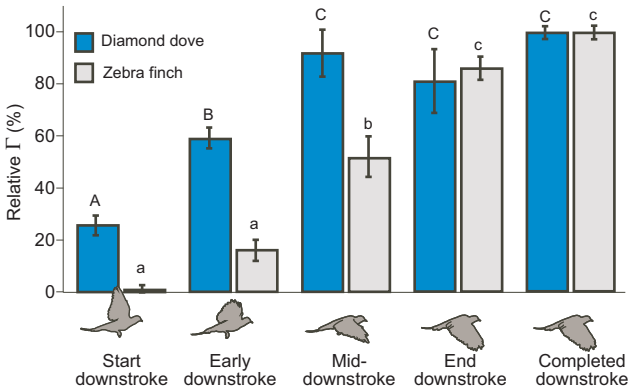

Fig. 8. Circulation during the wingbeat cycle in diamond doves and zebra finches. Circulation (Γ, m^2 s^{-1}) was standardized by dividing by the value of completed downstrokes previously left in the wake. Clap and peel increases circulation starting at the end of upstroke (the 'start downstroke' phase) in the dove, but not the finch. Data are means±s.e. Different letters represent statistically significant differences in mean circulation (P<0.05) within species (uppercase, doves; lowercase, finches). Circulation for each phase was statistically different between species (P<0.01) for all but the end of downstroke phase (P=0.94) and completed downstroke (P=0.97).

The Journal of Experimental Biology (2015) 218, 2518-2527 doi:10.1242/jeb.116228

previous model of the tip-reversal upstroke (Crandell and Tobalske, 2011) and kinematic measurements of whole-body acceleration that are consistent with an aerodynamically active upstroke in pigeons, a species that uses tip-reversal (Ros et al., 2011). Recent measurements in parrotlets (*Forpus coelestis*), a species that exhibits tip-reversal in slow flight, indicates minimal weight support; thrust was not measured (Lentink et al., 2015). This mechanism has the potential to contribute to decelerations during braking, perhaps via interactions with the wake of the previous downstroke. It may additionally contribute to weight support during hovering, although slight kinematic differences likely persist to re-orient flow. The generalities of this mechanism thus merit further study.

Through circulation and vorticity shed via wing–wing interactions, we interpret the clap and peel mechanism supplements circulation produced during downstroke. If this is the case, additional aerodynamic activity may supply additional thrust, potentially providing greater control during slow flight maneuverability (Ros et al., 2011). Further, clap and peel may generate a larger active area swept by the wings, and hence a greater whole-wingbeat span efficiency (Henningsson and Bomphrey, 2011, 2013; Henningsson et al., 2014; Muijres et al., 2011). However, before we can fully understand the details of time-varying force production and span efficiency, it will be essential to obtain better-resolved flow data. Our study will hopefully motivate new tests including time resolution and sampling either the Trefftz plane (Hedenström et al., 2007) or, alternatively, measurements directly on the wing (Muijres et al., 2008; Warrick et al., 2009). Such techniques would offer the opportunity to better estimate instantaneous forces. Further research of the wake flow is necessary using high-speed systems (Hedenström et al., 2009; Henningsson et al., 2011; Hubel et al., 2010) and whole-volume sampling (Bomphrey et al., 2012) to more fully elucidate the three-dimensional and time-varying nature of force production.

Our results add a new example of evolutionary convergence with insects and bats on the use of aerodynamic mechanisms. The clap and peel pattern resulting in a vortex shed in the sagittal plane and induced velocity directed posterior to the animal is consistent with the time-averaged aerodynamic flow pattern created by clap and fling in hawkmoths (Bomphrey et al., 2006). Thus, clap and peel joins leading edge vortices generated during the translational phase of wing movement and rotational circulation during wing reversal (Warrick et al., 2009) as examples of convergence with insects. Bats use a similar wingtip-reversal kinematic pattern during slow flight; however, the aerodynamic activity that has been observed occurs during the translational phase of the hand-wing, producing induced flow behind the animal similar to the flow measurements we have observed before the clap and peel in the dove (Hedenström et al., 2007). As such, bats have likely converged on a similar aerodynamic pattern during upstroke – the generality of the clap and peel in bats, however, remains untested.

Time-varying aerodynamic effects, most notably the leading edge vortex, have been demonstrated in gliding swifts (Videler et al., 2004), a slow flying flycatcher (Muijres et al., 2012a), and modeled in a large, flapping goose (Hubel and Tropea, 2010). Our study extends the understanding of the generality of such convergence across body sizes (and Reynolds numbers), meaning that time-varying aerodynamics are not limited to the smallest of vertebrate fliers (Muijres et al., 2008; Tobalske et al., 2009; Warrick et al., 2009). Diamond doves are 10× the mass of hummingbirds and nectarivorous bats.

The functional contribution of tip-reversal upstroke relative to flexed-wing upstroke begs the question of why it is that not all birds use the tip-reversal and clap and peel mechanisms. Addressing this question will require new insight into the various selective pressures that maintain rounded, low aspect ratio wings in birds. For example, rounded wings are thought to be more useful for avoiding wing damage in cluttered environments. In this context, it is noteworthy that Galliformes with rounded wings use tip-reversal when they are engaged in explosive escape flight after take-off (Tobalske and Dial, 2000). Another explanation was proposed by Vazquez (1992), who suggests there may be a trade-off in function between wrist-bone morphologies allowing a locked-in wing during glide versus those that facilitate the tip-reversal upstroke. In general, though, doves and pigeons glide when engaged in intermittent flight, whereas finches and related small passerines tend to flex their wings and bound (Tobalske, 2001). Further work examining the skeletal function using techniques such as XROMM (Brainerd et al., 2010) is necessary to test the 'wrist-lock' hypothesis (Vazquez, 1992).

Conclusions

It has long been recognized that bird species exhibit one of two general upstroke styles during slow flight (Brown, 1948), and here we have demonstrated detailed 3D kinematics and the aerodynamic consequences of these upstroke styles. The zebra finch uses a flexed-wing upstroke, and this upstroke period appears to produce a minimal aerodynamic trace. Diamond doves, with a wingtip-reversal upstroke, exhibit a clap and peel during the upstroke–downstroke transition that generates a shed vortex with measurable induced velocity added to the wake in a way that suggests thrust production that should help the bird progress on a forward path. Further work using time-resolved and volumetric PIV is necessary to refine this initial understanding of the aerodynamic contribution of the upstroke during slow-speed flight in birds.

MATERIALS AND METHODS

Animals and experimental design

Four diamond doves (*G. cuneata*, *Re*=51,000) and four zebra finches (*T. guttata*, *Re*=8500) were trained to fly between two perches positioned 2 m apart within a netted chamber (2×2×2 m) for all but the streamline experiment. For qualifying streamlines, birds flew in the working chamber of a variable-speed wind tunnel (0.6×0.6×0.8 m; see Tobalske et al., 1999, for details of the tunnel design). Information for the morphometrics of each bird is provided in Table 1; Reynolds number was calculated with mean flight velocity during kinematic trials and chord length is reported in Table 1. All procedures were approved by the Institutional Animal Care and Use Committee at the University of Montana.

Kinematics

We recorded wing and body motion using four high-speed video cameras – a Photron SA-3, two PCI 1024 s and a Phantom Miro Ex4, all synchronized using a TTL pulse. Recordings were made at 1000 Hz with a shutter speed of 1/10,000 s. Kinematic analyses of the wings and body during the third wingbeat following take-off were reconstructed in Matlab using a DLT conversion (Hedrick, 2008).

To quantify wing motion, we extracted the global angle of attack (α), global translational wingtip (V_T) and angular velocity (V_A) of the wing in global coordinates for a centroid of the hand-wing in both species (supplementary material Fig. S1). Additionally, to facilitate comparison between species, the wing cycle was divided into relative segments, with 0% and 100% defined as the start of upstroke based on wrist turn-around. The transition between upstroke and downstroke was defined visually at the directional reversal of the wing, and occurred at approximately 28 ms in the dove and 17 ms in the finch. For simplicity, and because we could not obtain time-resolved, whole-volume measures of flow velocity, we did not include induced velocity in our measures of α and V_T.

Several kinematic parameters were calculated for the hand-wing. To compare wing–wing contact, we digitized the wrist, wingtip (10th primary in the dove, 9th primary in the finch), first secondary feather and last secondary feather for both the left and right wing. To compare distances between different points on the wing, we calculated the linear distance between each contralateral point on the corresponding left and right wing.

For additional kinematic parameters, we utilized an average location of the hand-wing. We calculated a hand-wing centroid by averaging the x, y and z position of the wrist, 10th primary (dove) or 9th primary (finch), and the 3rd primary on the left wing. For all parameters presented, we used global coordinates (i.e. not bird-centered). Supplementary material Fig. S1 illustrates each variable described herein. α was calculated by measuring the angle between the hand-wing centroid's velocity vector and a wing chord approximated as a line between the wrist and first secondary feather (approximating a flat wing). V_T (m s^{-1}) was calculated with the direct linear distance between the centroid from frame to frame per unit time (1 ms apart). V_A, or rotational velocity, was calculated as the angle between the hand-wing centroid position vector relative to the shoulder in subsequent frames (1 ms). For all parameters, means and standard deviations across individuals were calculated.

PIV

We used a PIV system (LaVision GmBH, Goettingen, Germany) with DaVis 7.1 software. A dual-cavity pulsed 50 mJ Nd:YAG laser was used to illuminate a 2 mm thick flow field, with planar dimensions spanning a field of approximately 35×25 mm. The laser was oriented behind the flight trajectory, leaving the animal's head in a shadow, so as not to damage its eyes. We seeded the air with particles of olive oil less than 1 µm in diameter, generated at a rate of 7×10^{10} particles s^{-1} using a vaporizer fitted with a Laskin nozzle. Particle illumination was recorded using a 1376×1040 pixel charged-coupled device (CCD) camera placed perpendicular to the illumination field. To calculate particle velocity, we used cross-correlation of paired images with an elapsed time between images of 500 µs. We used a multi-pass filter with an initial interrogation area of 64×64 pixels and a final area of 16×16 pixels with 50% overlap.

We calculated velocity (m s^{-1}), vorticity (ω, s^{-1}) and circulation (Γ, m^2 s^{-1}) as described in Warrick et al. (2009) and Provini et al. (2014). Briefly, we integrated all same-sign ω in a given PIV field within 1.5 chord lengths of peak ω to measure Γ. We considered each negatively signed vortex core deposited in the wake during downstroke to represent the cross-section of an elliptical vortex ring shed from the trailing edge from the wing. In the case of Γ deposited in the wake due to upstroke, we used a visual cut-off of streamlines to quantify the presence of Γ (see fig. 3 in Provini et al., 2012). This anomalous vorticity was considered to be created from the motion of the upstroke during the wing-tip reversal upstroke and is likely the result of vorticity shed from the wingtip. Average free-stream background vorticity was measured at 0.006±0.008 s^{-1}, 1.5% of average peak vorticity measured in the wake for the birds. Thus, we applied no masking. Added mass of the vortex wake was not calculated, as we lacked adequate time resolution to measure displacement of shed vortices (Dabiri, 2005). It has been previously shown in chukar partridge (*Alectoris chukar*) that birds generate negligible aerodynamic added mass (Tobalske and Dial, 2007).

We sampled the near-wake of the birds in a parasagittal plane (±1 cm from sagittal plane). Samples were taken at 5 Hz, and were recorded during the initial 3rd to 5th wingbeat after takeoff from a perch, at body velocities of approximately 3 m s^{-1} for the doves and 1.5 m s^{-1} for the finches. To quantify growth in Γ with respect to time, we divided the wingbeat into four phases: (1) transition from upstroke to downstroke (dove N=19, finch N=9; approximately 40–50% of the entire wingbeat cycle; Figs 2, 3); (2) first quarter of downstroke (dove N=30, finch N=16; approximately 50–63% of the wingbeat cycle); (3) second quarter of downstroke (dove N=20, finch N=13; approximately 63–75% of the wingbeat cycle); and (4) third and fourth quarters of downstroke (dove N=14, finch N=21; approximately 75–100% of the wingbeat cycle) based on wingtip elevation and depression relative to the bird. We measured previously shed downstroke Γ left in the wake for comparison with the most recently completed wingbeat (dove N=124, finch N=82). We tested for differences in the time course of circulation between birds using a one-way ANOVA, with individual as a factor, and found no differences in mean downstroke force production among individuals (for doves: $0.76<P<0.99$, for finches: $0.33<P<0.98$); thus, all birds were combined for final analyses. Herein, we report means±s.d. To compare phases within species, we used a one-way ANOVA with phase as a factor, followed by a Tukey *post hoc* test to determine significant differences between phases. To compare the percentage circulation during each phase between species, we used a Student's t-test.

Time-resolved flow

To more fully observe flow characteristics with respect to time and volume, we employed a classic smoke streamline study (Barlow et al., 1999; Ellington et al., 1996). We installed a nichrome wire (60 gauge) horizontally across the front of the working section of a variable speed wind tunnel (Tobalske et al., 1999). This wire was connected to a 15 V power supply. We seeded the wire with mineral oil droplets approximately 0.5 cm apart. When current was applied to the wire, it produced heat, and the droplets burnt to create streamlines. For these experiments, air velocity in the tunnel was 0.95±0.05 m s^{-1}. One dove and one finch were flown within the tunnel, and the flight and smoke flow were recorded from a dorsal view using a Photron PCI 1024 high-speed camera recording at 1000 frames s^{-1}, with a shutter speed of 1/5000 s.

Force estimates

To gain an approximation of body weight support provided by the aerodynamic mechanisms we observed, we utilized two models. To estimate net force during the downstroke, we used a momentum jet model, as described by Vogel (1994):

$$F = \rho\Gamma A/T. \quad (1)$$

We used this calculation for each quarter of the downstroke divided equally by time (T=9.25 ms), with corresponding measures of Γ (see Fig. 8) and swept wing area A, for each quarter, where air density ρ=1.07 kg m^{-3} in Missoula, MT, USA. We then averaged the momentum jet model calculated for each section, for a net force estimate.

As a rough estimate of potential force production of the clap phase, we elected to use the reverse peel model (Miller and Peskin, 2009). This estimation was only possible for the dove, as the finch did not have a kinematic pattern close to a clap and peel, and so we could not estimate the angle between the two wings. The reverse peel is modeled as:

$$F = \rho\beta c u^2, \quad (2)$$

where β is the estimated angle between the two wings for the last 10 ms of the clap (approximately 50 deg in the dove), c is the wing chord and u is the average airspeed resulting from the clap (Fig. 7).

Acknowledgements

We would like to thank Heather Labbe for assistance with data collection, and Andy Biewener, Tom Brekke, Doug Emlen, Art Woods, the UMT Morphology Group and anonymous reviewers for valuable insight.

Competing interests

The authors declare no competing or financial interests.

Author contributions

Both authors were involved in the research design, interpretation of findings and preparation of the manuscript. K.E.C. additionally performed the experiments and analyzed the data.

Funding

K.E.C. was funded by a NASA-Montana Space Grant Consortium (MSGC) Graduate Research Fellowship and this work was also funded by National Science Foundation Grants IOS-0923606 and IOS-0919799.

Supplementary material

Supplementary material available online at
http://jeb.biologists.org/lookup/suppl/doi:10.1242/jeb.116228/-/DC1

References

Barlow, J., Rae, W. and Pope, A. (1999). *Low-Speed Wind Tunnel Testing*. Canada: John Wiley & Sons.

Bennett, L. (1977). Clap and fling aerodynamics - experimental evaluation. *J. Exp. Biol.* **69**, 261-272.

Berg, A. M. and Biewener, A. A. (2010). Wing and body kinematics of takeoff and landing flight in the pigeon (*Columba livia*). *J. Exp. Biol.* **213**, 1651-1658.

Bomphrey, R. J., Lawson, N. J., Taylor, G. K. and Thomas, A. L. R. (2006). Application of digital particle image velocimetry to insect aerodynamics: measurement of the leading-edge vortex and near wake of a Hawkmoth. *Exp. Fluids* **40**, 546-554.

Bomphrey, R. J., Henningsson, P., Michaelis, D. and Hollis, D. (2012). Tomographic particle image velocimetry of desert locust wakes: instantaneous volumes combine to reveal hidden vortex elements and rapid wake deformation. *J. R. Soc. Interface.* **9**, 3378-3386.

Brainerd, E. L., Baier, D. B., Gatesy, S. M., Hedrick, T. L., Metzger, K. A., Gilbert, S. L. and Crisco, J. J. (2010). X-Ray reconstruction of moving morphology (XROMM): precision, accuracy, and applications in comparative biomechanics research. *J. Exp. Zool.* **313A**, 262-279.

Brown, R. H. J. (1948). The flight of birds - the flapping cycle of the pigeon. *J. Exp. Biol.* **25**, 322-333.

Brown, R. H. J. (1953). The flight of birds 2. Wing function in relation to flight speed. *J. Exp. Biol.* **30**, 90-103.

Brown, R. H. J. (1963). The flight of birds. *Biol. Rev. Camb. Philos. Soc.* **38**, 460-489.

Chang, Y.-H., Ting, S.-C., Su, J.-Y., Soong, C.-Y. and Yang, J.-T. (2013). Ventral-clap modes of hovering passerines. *Phys. Rev. E* **87**, 022707.

Corning, W. R. and Biewener, A. A. (1998). *In vivo* strains in pigeon flight feather shafts: implications for structural design. *J. Exp. Biol.* **201**, 3057-3066.

Crandell, K. E. and Tobalske, B. W. (2011). Aerodynamics of tip-reversal upstroke in a revolving pigeon wing. *J. Exp. Biol.* **214**, 1867-1873.

Dabiri, J. O. (2005). On the estimation of swimming and flying forces from wake measurements. *J. Exp. Biol.* **208**, 3519-3532.

Dial, K. P. (1992). Activity patterns of the wing muscles of the pigeon (*Columba livia*) during different modes of flight. *J. Exp. Zool.* **262**, 357-373.

Dudley, R. (2000). *The Biomechanics of Insect Flight*. NJ, USA: Princeton University Press.

Earls, K. D. (2000). Kinematics and mechanics of ground take-off in the starling *Sturnis vulgaris* and the quail *Coturnix coturnix*. *J. Exp. Biol.* **203**, 725-739.

Ellington, C. (1975). Non-steady state aerodynamics of the flight of *Encarsia formosa*. In *Swimming and Flying in Nature* (ed. T. W.-T. Wu, C. J. Brokaw and C. Brennen). New York, NY, USA: Plenum Press.

Ellington, C. P. (1984). The aerodynamics of hovering insect flight. IV. Aerodynamic mechanisms. *Philos. Trans. R. Soc. Lond. B Biol. Sci.* **305**, 79-113.

Ellington, C. P., Van Den Berg, C., Willmott, A. P. and Thomas, A. L. (1996). Leading-edge vortices in insect flight. *Nature* **384**, 626-630.

Hedenström, A., Rosén, M. and Spedding, G. R. (2006). Vortex wakes generated by robins *Erithacus rubecula* during free flight in a wind tunnel. *J. R. Soc. Interface* **3**, 263-276.

Hedenström, A., Johansson, L. C., Wolf, M., von Busse, R., Winter, Y. and Spedding, G. R. (2007). Bat flight generates complex aerodynamic tracks. *Science* **316**, 894-897.

Hedenström, A., Muijres, F. T., von Busse, R., Johansson, L. C., Winter, Y. and Spedding, G. R. (2009). High-speed stereo DPIV measurement of wakes of two bat species flying freely in a wind tunnel. *Exp. Fluids* **46**, 923-932.

Hedrick, T. L. (2008). Software techniques for two- and three-dimensional kinematic measurements of biological and biomimetic systems. *Bioinspir. Biomim.* **3**, 034001.

Hedrick, T. L., Usherwood, J. R. and Biewener, A. A. (2004). Wing inertia and whole-body acceleration: an analysis of instantaneous aerodynamic force production in cockatiels (Nymphicus hollandicus) flying across a range of speeds. *J. Exp. Biol.* **207**, 1689-1702.

Henningsson, P. and Bomphrey, R. J. (2011). Time-varying span efficiency through the wingbeat of desert locusts. *J. R. Soc. Interface*, rsif20110749.

Henningsson, P. and Bomphrey, R. J. (2013). Span efficiency in hawkmoths. *J. R. Soc. Interface* **10**, 20130099.

Henningsson, P., Muijres, F. T. and Hedenstrom, A. (2011). Time-resolved vortex wake of a common swift flying over a range of flight speeds. *J. R. Soc. Interface* **8**, 807-816.

Henningsson, P., Hedenström, A. and Bomphrey, R. J. (2014). Efficiency of lift production in flapping and gliding flight of swifts. *PLoS ONE* **9**, e90170.

Hubel, T. Y. and Tropea, C. (2010). The importance of leading edge vortices under simplified flapping flight conditions at the size scale of birds. *J. Exp. Biol.* **213**, 1930-1939.

Hubel, T. Y., Riskin, D. K., Swartz, S. M. and Breuer, K. S. (2010). Wake structure and wing kinematics: the flight of the lesser dog-faced fruit bat, Cynopterus brachyotis. *J. Exp. Biol.* **213**, 3427-3440.

Lehmann, F.-O., Sane, S. P. and Dickinson, M. (2005). The aerodynamic effects of wing-wing interaction in flapping insect wings. *J. Exp. Biol.* **208**, 3075-3092.

Lentink, D., Haselsteiner, A. F. and Ingersoll, R. (2015). In vivo recording of aerodynamic force with an aerodynamic force platform: from drones to birds. *J. R. Soc. Interface* **12**, 20141283.

Lorenz, K. (1933). Beobachtetes über das Fliegen der Vögel und über die Beziehungen der Flügel- und Steuerform zur Art des Fluges. *J. Ornithol.* **81**, 107-236.

Marey, E. (1890). *Locomotion Dans L'air*. In *Le Vol Des Oiseaux*. Paris, France: Le Mouvement.

Maxworthy, T. (1979). Experiments on the Weis-Fogh mechanism of lift generation by insects in hovering flight. Part 1. Dynamics of the 'fling'. *J. Fluid Mech.* **93**, 47.

Miller, L. A. and Peskin, C. S. (2009). Flexible clap and fling in tiny insect flight. *J. Exp. Biol.* **212**, 3076-3090.

Muijres, F. T., Johansson, L. C., Barfield, R., Wolf, M., Spedding, G. R. and Hedenstrom, A. (2008). Leading-edge vortex improves lift in slow-flying bats. *Science* **319**, 1250-1253.

Muijres, F. T., Spedding, G. R., Winter, Y. and Hedenström, A. (2011). Actuator disk model and span efficiency of flapping flight in bats based on time-resolved PIV measurements. *Exp. Fluids* **51**, 511-525.

Muijres, F. T., Bowlin, M. S., Johansson, L. C. and Hedenstrom, A. (2012a). Vortex wake, downwash distribution, aerodynamic performance and wingbeat kinematics in slow-flying pied flycatchers. *J. R. Soc. Interface* **9**, 292-303.

Muijres, F. T., Johansson, L. C., Bowlin, M. S., Winter, Y. and Hedenström, A. (2012b). Comparing aerodynamic efficiency in birds and bats suggests better flight performance in birds. *PLoS ONE* **7**, e37335.

Muijres, F. T., Johansson, L. C. and Hedenström, A. (2012c). Leading edge vortex in a slow-flying passerine. *Biol. Lett.*, rsbl20120130.

Pournazeri, S., Segre, P. S., Princevac, M. and Altshuler, D. L. (2013). Hummingbirds generate bilateral vortex loops during hovering: evidence from flow visualization. *Exp. Fluids* **54**, 1439.

Provini, P., Tobalske, B. W., Crandell, K. E. and Abourachid, A. (2012). Transition from leg to wing forces during take-off in birds. *J. Exp. Biol.* **215**, 4115-4124.

Provini, P., Tobalske, B. W., Crandell, K. E. and Abourachid, A. (2014). Transition from wing to leg forces during landing in birds. *J. Exp. Biol.* **217**, 2659-2666.

Ros, I. G., Bassman, L. C., Badger, M. A., Pierson, A. N. and Biewener, A. A. (2011). Pigeons steer like helicopters and generate down- and upstroke lift during low speed turns. *Proc. Natl. Acad. Sci. USA* **108**, 19990-19995.

Sane, S. P. (2003). The aerodynamics of insect flight. *J. Exp. Biol.* **206**, 4191-4208.

Scholey, K. D. (1983). Developments in vertebrate flight: climbing and gliding of mammals and reptiles, and the flapping flight of birds. PhD thesis, University of Bristol, UK.

Simpson, S. F. (1983). The flight mechanism of the pigeon *Columbia livia* during take-off. *J. Zool.* **200**, 435-443.

Spedding, G. R. and Hedenström, A. (2009). PIV-based investigations of animal flight. *Exp. Fluids* **46**, 749-763.

Spedding, G. R., Hedenström, A. and Rosén, M. (2003a). Quantitative studies of the wakes of freely flying birds in a low-turbulence wind tunnel. *Exp. Fluids* **34**, 291-303.

Spedding, G. R., Rosén, M. and Hedenström, A. (2003b). A family of vortex wakes generated by a thrush nightingale in free flight in a wind tunnel over its entire natural range of flight speeds. *J. Exp. Biol.* **206**, 2313-2344.

Tobalske, B. W. and Dial, K. P. (1996). Flight kinematics of black-billed magpies and pigeons over a wide range of speeds. *J. Exp. Biol.* **199**, 263-280.

Tobalske, B. W. (2001). Morphology, velocity, and intermittent flight in birds. *Amer. Zool.* **41**, 177-187.

Tobalske, B. W. (2007). Biomechanics of bird flight. *J. Exp. Biol.* **210**, 3135-3146.

Tobalske, B. W. and Dial, K. P. (2000). Effects of body size on take-off flight performance in the Phasianidae (Aves). *J. Exp. Biol.* **203**, 3319-3332.

Tobalske, B. W. and Dial, K. P. (2007). Aerodynamics of wing-assisted incline running in birds. *J. Exp. Biol.* **210**, 1742-1751.

Tobalske, B. W., Peacock, W. L. and Dial, K. P. (1999). Kinematics of flap-bounding flight in the zebra finch over a wide range of speeds. *J. Exp. Biol.* **202**, 1725-1739.

Tobalske, B. W., Hedrick, T. L., Dial, K. P. and Biewener, A. A. (2003). Comparative power curves in bird flight. *Nature* **421**, 363-366.

Tobalske, B. W., Hearn, J. W. D. and Warrick, D. R. (2009). Aerodynamics of intermittent bounds in flying birds. *Exp. Fluids* **46**, 963-973.

Vazquez, R. J. (1992). Functional osteology of the avian wrist and the evolution of flapping flight. *J. Morphol.* **211**, 259-268.

Videler, J. J., Stamhuis, E. J. and Povel, G. D. E. (2004). Leading-edge vortex lifts swifts. *Science* **306**, 1960-1962.
Vogel, S. (1967). Flight in drosophila 3. Aerodynamic characteristics of fly wings and wing models. *J. Exp. Biol.* **46**, 431.
Vogel, S. (1994). *Life in Moving Fluids: The Physical Biology of Flow*. Princeton, NJ: Princeton University Press.
Warrick, D. R., Tobalske, B. W. and Powers, D. R. (2005). Aerodynamics of the hovering hummingbird. *Nature* **435**, 1094-1097.
Warrick, D. R., Tobalske, B. W. and Powers, D. R. (2009). Lift production in the hovering hummingbird. *Proc. R. Soc. B Biol. Sci.* **276**, 3747-3752.
Weis-Fogh, T. (1973). Quick estimates of flight fitness in hovering animals, including novel mechanisms for lift production. *J. Exp. Biol.* **59**, 169-230.

Skeletal kinematics of the avian wing during slow flight

Abstract

During slow flight, birds exhibit predictable downstroke kinematics, but have one of two upstroke styles. These styles contribute to differences in aerodynamic force production, and so overall variation flight performance. The functional difference between upstrokes has been explained with variation in underlying skeletal morphology. Birds with an aerodynamically active "wingtip-reversal" upstroke style tend to exhibit greater distal muscle mass and more robust wing skeletal elements, in comparison to birds with the aerodynamically inactive "flexed-wing" upstroke style. Here, we address the hypothesis that the underlying skeletal morphology reflects differences in internal skeletal kinematics in two species: the Rock dove (wing-tip reversal upstroke) and the European starling (flexed-wing upstroke). We animate skeletal motion with XROMM (X-ray Reconstruction of Moving Morphology) to examine the contributions of each skeletal element of the wing: the contribution of the humerus, radius/ulna, and manus in turn. We find that both kinematic styles exhibit similar skeletal kinematic patterns, but differ significantly in magnitude and timing of joint excursion. Notable exceptions to the similarities include high long-axis rotation of the manus during upstroke in the pigeon, which contributes heavily to overall wing pronation, while the starling exhibits negligible long-axis rotation at the wrist. In contrast, higher pronation in the ulna/radius is apparent in the starling during upstroke. Together, these two

exceptions coupled with differences in timing and excursion angles explain variation in upstroke patterns.

Keywords: XROMM, bird flight, wrist, manus, long axis rotation, wingtip-reversal upstroke

Introduction

Birds capitalize on a suite of aerodynamic mechanisms to enhance force production during flight. During slow flight, birds are aerodynamically challenged, as most (if not all) of the induced velocity necessary to remain aloft and accelerate must be produced by the bird, rather than by redirecting existing airflow. Unsurprisingly, this phase is the most energetically costly phase of aerial locomotion for birds (Tobalske *et al.* 2003). To improve force production during this phase, birds with long, pointed wings use a 'wingtip-reversal upstroke.' These birds capitalize on a clap and fling mechanism during the transition from upstroke to downstroke (Crandell & Tobalske 2015) and induced momentum to the wake during mid-upstroke (Crandell & Tobalske 2011; Crandell & Tobalske 2015). In contrast, birds with rounded wings have a 'flexed-wing upstroke,' and do not capitalize on additional force production during the upstroke (Crandell & Tobalske 2015), with the notable exception of the Phasianidae (Tobalske & Dial 2000).

48 The aerodynamic signature of both wingbeat styles appears closely tied to
49 the external wing kinematics in Diamond doves and Zebra finch (Crandell &
50 Tobalske 2015). However, the musculo-skeletal contribution to these motions
51 remain unknown. Because birds that produce a flexed-wing upstroke have short,
52 rounded wings, these wings exhibit proportionally less momentum during upstroke.
53 It is possible that birds with different external kinematic patterns utilize similar
54 skeletal kinematic patterns, but the resulting external wing motions are drastically
55 different between upstroke styles, as momentum may dominate a long, pointed
56 wing.
57 Avian upstrokes may be actively controlled, or a by-product of wing shape.
58 Support for a muscularly-powered wingtip-reversal upstroke appears in both the
59 muscle (Corvidae, Bierregaard & Peters 2006) and skeletal (Dial 1992b)
60 morphology in comparative analyses. Specifically, birds that appear to use unsteady
61 aerodynamic mechanisms more often have a different forelimb skeletal morphology.
62 The ratio between humerus and ulna lengths correlates with three roughly defined
63 classes of flight kinematics, form steady to unsteady (Nudds 2007). Similarly,
64 forelimb skeletal elements appear to be more robust in species that utilize unsteady
65 mechanisms. The radius and ulna bend away from each other, suggested to
66 accommodate relatively large distal muscles (see Fig. 7 in (Dial 1992b)). Direct
67 measures of musculature in three hawk species support this idea: Opsrey (*Pandion*
68 *haliaetus*), a species observed with a pronounced tip-reversal upstroke during
69 foraging, has a significantly larger supinator muscle than two other species
70 (Corvidae, Bierregaard & Peters 2006), after accounting for between-species size

differences. Muscles that insert on the most distal skeletal elements, the manus, appear to follow the fine control of the hand-wing (Vazquez 1995). In fact, the pigeon is unable to take off and struggles in landing without the use of the antebrachial muscles (Dial 1992b). These anatomical observations suggest that direct muscular control of the distal wing is critical during acceleration and deceleration.

In contrast, (Vasquez 1992) suggests that upstroke patterns are a consequence of skeletal morphology and do not require the distal muscles. Vazquez proposes that a passive skeletal mechanism is responsible for the supination of the manus. From a morphological analysis of duck (*Anseriformes*) wrist bones, he outlines the following prediction for supination: First, the ulnocarpo-metacarpal ligament is brought under tension. Then, due to this tension, the ventral ridge of the manus slides along the ulnare, causing the wing to flick (Vasquez 1992). This proposed mechanism remains entirely passive, with negligible muscle input to produce the dramatic supination.

Here, we explore skeletal contributions to the two distinct avian upstroke styles, using an XROMM (X-ray Reconstruction of Moving Morphology) analysis. We describe movement along the six degrees of freedom for each of the major skeletal elements of the avian wing, in order to compare the general motions of the wingtip-reversal and flexed-wing upstroke style.

Methods

Birds & Surgical Procedures

Three captive-bred pigeons (*Columba livia*; Kate Davis, Raptors of the Rockies) and three wild-caught European starlings (*Sturnus vulgaris*; Fort Missoula Research Station, Missoula, MT) were used in this study. Pigeons were trained for two weeks prior to surgical procedure to cue in on a white platform to land. Starlings were trained for four weeks prior to procedures to cue in on a cylindrical (rod) perch at the end of a mesh tunnel. Reported herein are values for one pigeon (mass 262 grams) and three starlings (mass 68.0 ± 2.8 grams).

Surgical procedures were done at the Field Research Station at Fort Missoula (Missoula, MT, USA). Birds were anesthetized using inhaled isofluorane (HME109, 5% to induce, 2-3% to maintain; Highland Medical Equipment, Temecula, CA, USA). Feathers were removed as needed over the incision sites. At each incision site, the skin was manipulated to maximize access to a given location along the skeleton. Incisions were made at the keel, dorsal proximal end of the humerus, ventral distal end of the humerus (includes access to the proximal ulna), and the dorsal and ventral wrist. Implantation directly in to the distal carpometacarpus was possible without incision beyond the use of the drill. Skeletal implants consisted of 0.8 or 0.5 mm diameter tantalum beads (BalTec, Los Angeles, CA). Implantation holes were drilled directly in to the bone with drill bits (of width 0.09 or 0.06 mm; McMaster Carr) mounted in insect pin holders. Incisions were closed with suture (0-3 or 0-4 silk), or in instances of small incisions, vet-bond. Post-surgery birds were kept in a

small heated cages (food and water *ad libitum*) to recover for the first 6 hours, heat was removed after six hours. After 24 hours, birds were examined and moved back to aviaries. Birds were given one to two weeks recovery time before flight trials. All procedures approved by the University of Montana Institutional Animal Care and Use Committee (IACUC).

Flight Trials

Trials were video recorded at the W. M Keck Foundation XROMM (X-ray Reconstruction of Moving Morphology) Lab at Brown University (Providence, RI). Birds were flown between two Varian model G-1086 x-ray tubes and two Dunlee model TH9447QXH590 image intensifiers. Video outputs on the image intensifiers were recorded using two Phantom v10 high-speed cameras (1760x1760 pixels). Cameras were synced via a TTL pulse and sampled at 500 frames per second, with a shutter speed of 1/5,000 s. Both pigeons and starlings were flown through a constructed mesh corridor with a white platform (pigeons) or perch (starlings) at the end. To time releases to x-ray operation, birds were released by hand and flew two to three wingbeats before flying between intensifiers.

The three-dimensional interrogation volume was calibrated via standard XROMM Keck lab methods (xromm.org). Briefly, image distortion was accounted for by taking an image with a perforated metal grid taped to the image intensifier. The "undistortion" program (xromm.org) was used to create a transformation matrix. This matrix was applied to all subsequent images (calibration and trial). Calibrations were done using the Keck lab large cube.

CT scans and skeletal models

Following locomotor trials, all birds were euthanized. Bird carcasses were scanned at Brown University with the Keck Foundation CT-scanner (Fidex Veterinary CT scanner) (Starling slice thickness 0.199701, 80KvP, 43 mA; Pigeon slice thickness 0.216342, 80 KvP, 43 mA). Each bone was segmented out in Osirix software (32-bit) and saved as polygonal mesh models. Marker models for each bone segment were additionally saved as polygonal mesh models. Bone models were linked to marker models in Maya.

Animation

To measure the precision of our data, inter-marker distances were calculated for pairs of markers within the same bone (Figure 1, table 1). This approximation assumes negligible bone deformation during locomotion, and that the manus is treated as a unit (while it is composed of the carpometacarpus, phalanx 1 and phalanx 2). From 10 pairs of markers, the lowest standard deviation was 0.078 mm between point 1 and 4 of the trunk. The highest standard deviation was 0.17 mm between point 14 and 18 of the manus (Table 1). Notably, point 14 resides on the carpometacarpus, while point 18 was on the phalanx 3.

Marker coordinates from direct linear transformed data were filtered using a low-pass Butterworth filter with a 25 Hz cutoff frequency. Filtered markers were used to calculate rigid-body translations and rotations (see (Brainerd *et al.* 2010)). Rigid body transformations were applied to mesh bone models in Autodesk Maya

(2012, Autodesk Inc., San Rafael, CA, USA) using the XROMM package. One-marker rotoscoping was employed for the pigeon ulna. Two-marker rotoscoping was employed for all the starling ulnas and trunks.

Data Analysis

To describe motion around the wing joints, kinematic data were extracted in Maya using joint coordinate systems (Figure 2). The wrist joint represents motion of the carpometacarpus relative to the radius and ulna. The elbow joint represents motion of the radius and ulna relative to the humerus. For all joints, the radius and ulna were treated as a single fixed bone, when in reality slight motion between the radius and ulna may exist. Likewise, the manus was treated as one discrete element (including the carpometacarpus and phalanx 2 and 3). Additionally, the trunk was treated as a single solid object, and included the spinal column, pelvic, and pectoral girdles. This eliminated our ability to accommodate for changes in compression of the furcula – known to move up to 129% wider from resting length (Baier, Gatesy & Dial 2013). Our 'zero' position was selected as mid-downstroke posture - all reported values herein are relative to the bone positions in mid-downstroke (Figure 2) for both species. In general, our placements of joint coordinate systems followed the conventions of Baier et al. (2013). Briefly, these systems follow the inertial axes of the bone, wherein the z axis (blue, Figure 2) experiences the highest inertia of the more distal bone in the joint, and the x-axis, the lowest. Thus, the z-axis generally followed the ab- and adduction plane (although at the shoulder, it followed flexion-extension), and the x-axis follows the long-axis rotation of the distal long bone. The

y-axis lies perpendicular to both. One notable exception to Baier et al. (2013) is that our study focuses on the long axis rotation of the long bones, an axis that is traditionally prioritized last (but see (Kambic, Roberts & Gatesy 2014)). Thus, our joint coordinate systems prioritized the long axis rotation axis over the ab- and adduction axis, which remains perpendicular to long-axis rotation.

Wingbeat timing was identified as being at the turn-around of the distal wingtip in both x-ray views. A slight delay between skeletal and feather turn-around may exist, and so we suggest interpreting comparisons with external kinematics with caution due to uncertainty about the precise upstroke-downstroke transition moment (see Baier, Gatesy & Dial 2013).

In order to measure how each joint contributes to the whole wing motion in both species, we modified the methods of Hedrick et al. (2012) and Baier et al. (2013). We created a tip trace for the distal-most point on the carpometacarpus, and tracked it throughout a complete wingbeat cycle, with coordinates centered at the shoulder joint. We then removed all motion due to the humerus, and then the radius/ulna. The traces remaining are motion due just to the motion of the bones distal to the targeted bone. For example, tip traces for the ulna include motion of the ulna and the manus, while tip traces for the manus include only motion of the manus.

Results

We found several differences between the pigeon and starling kinematics during a single wingbeat cycle. We find that the tip reversal upstroke is largely due

to pronation of the hand-wing, skeletally accomplished with long axis rotation of the manus at the wrist joint. In contrast, the flexed-wing upstroke in the starling is largely accomplished by flexion and long-axis rotation at the elbow joint.

Wrist Joint Kinematics

During the upstroke in the pigeon, a majority of the carpometacarpus (CMC) motion was due to the long axis rotation of the bone (Fig. 3A). During the upstroke, the wrist supinates, and then pronates during the wingtip-reversal upstroke. During the upstroke, the manus undergoes a long axis rotation of 79.2° (the difference between the maximum and minimum values during upstroke are reported herein). During the downstroke, long axis rotation is reduced, moving through 49.4°. A majority of that occurs as the manus continues to pronate at the transition between upstroke and downstroke. The manus then gradually supinates throughout downstroke.

In contrast, the starling manus goes through a smaller long axis rotation during upstroke, moving 16.4° (from -0.5 ± 4.3° to 15.8 ± 1.5°) during upstroke (Fig 3D). A majority of this motion occurs early in the upstroke, where the CMC pronates before it is abducted (Fig. 3E). However, it is supinated, and during the last half of the upstroke (25-50% of the total stroke cycle) the wing undergoes negligible long-axis rotation.

The manus in the pigeon goes through minimal abduction during upstroke (up to 34.0° at the upstroke-downstroke transition), suggesting this motion is due to

a more proximal skeletal element (Fig 3E). In contrast, the starling manus is abducted heavily, abducting 33.0° (from -39.4 ± 16.6° to -6.4 ± 7.5°) (Fig 3E) while the wing is flexed 66.6° (from -87.4 ± 47.3° to –20.8 ± 23.2°) toward the body (Fig 3F). The pigeon flexes the manus at the wrist 47.4° - consistent with the hand-wing remaining extended, but flexed toward the body.

In addition to the joint coordinate system, we qualitatively addressed the interaction between the carpometacarpus and the wrist bone, the ulnare (or cuneiform). We find visual confirmation that there is an interaction between the ventral ridge of the carpometacarpus and the ventral ramus of the ulnare during the tip-reversal portion of the upstroke (25-50% of wingbeat cycle; Supplemental Video 1).

Elbow Joint Kinematics

During the upstroke in the pigeon, the ulna pronates 44.9° (Fig 4A) as the manus supinates (Fig 3A). Before downstroke, the ulna supinates back to end of downstroke values. The starling follows a similar pattern, pronating 92.3° during the first half of upstroke (0-25% of wingbeat cycle; from 8.3 ± 28.5° to 84.0 ± 42.1°). During downstroke, the pigeon does not go through much long-axis rotation at the elbow. Over the course of the entire downstroke (50-100% of the wingbeat cycle), the starling supinates through 50.3° (from 38.7 ± 23.9° at the start of downstroke to -11.6 ± 8.2° at the end of downstroke).

In both the pigeon and starling, the elbow abducts through the first half of upstroke (Fig 4B, 4E) (0-25% wingbeat cycle), and then adducts for the second half (25-50% of the wingbeat cycle), prior to downstroke. The starling goes through an arc (28.8° - from 36.2 ± 22.6° to 7.4 ± 7.7°) approximately that of the pigeon (45.5°). During downstroke, the elbow joint remains constant – neither abducting nor adducting heavily for both birds.

Levels of flexion and extension of the elbow joint (Fig. 4C, F) are comparable for the pigeon and starling. The starling flexes and extends the ulna and radius between -95.6 ± 44.6° and -40.1 ± 35.2°, a path of 55.6°. The pigeon flexes from 3.5° to a maximum of 35.1°, a total arc of 38.5°.

Shoulder Joint Kinematics

During the upstroke, the pigeon humerus supinates 98.3° rapidly at 25-30% through the wingbeat cycle (Figure 5A). This occurs at the same time as the carpometacarpus begins to pronate, although during a shorter duration (pronation occurs approximately 20% of the wingbeat cycle). Following this supination, the humerus remains heavily supinated throughout the 'clap' and in to the 'peel' upstroke-downstroke transition. For the starling, a similar pattern of long axis rotation (Figure 5D), to a lesser degree, occurs during the first 33% of the wingbeat cycle, supinating through 44.7° - from -22 ± 16.7° to -67.6 ± 28.1°.

During this rapid supination in the pigeon, the humerus also abducts 146.1° quickly to extend the wing dorsally, setting the bird up for the 'clap and peel'

upstroke to downstroke transition (Figure 5B). In the starling, a similar pattern of long axis rotation, covering 130.1°, from -43.6 ± 21.2° to 87.3 ± 43.9 ° occurs over a much longer time interval (approximately 40% of the wingbeat cycle).

The pigeon humerus flexes toward the body throughout the initial 33% of the upstroke, flexing 85.5° (Fig. 5C). In contrast, the starling flexes toward the body at a much lower angle, 44.9° (Fig 5F; from -12.7 ± 10.6° to -57.6 ± 37.3°).

Joint contributions to whole-wing motion

In the pigeon, we found that the shoulder is responsible for a majority of the cranial-caudal motion of the wingtip (86% of wingbeat, Figure 6B, E). In contrast, the elbow contributes most to dorso-ventral motion of the wing (94% of wingbeat, Figure 6C). The wrist joint contributes most to motion in the lateral plane (68%, Figure 6G).

For the starling, the shoulder is the dominant joint responsible for cranial-caudal motion (48% of all motion centered at the shoulder), as well as dorso-ventral motion (44%). The wingtip-trace of isolated wrist motion follows the same general pattern (to a lesser degree) as the shoulder joint in the lateral view. However, the amount of flexion is much reduced at the wrist – indicating that the flexion of the elbow joint is crucial for the flexed-wing upstroke. In fact, the elbow joint dominates all flexion of the wingtip (Figure 7E).

Discussion

We have established that the skeletal kinematics in birds during slow flight is different between the two upstroke styles. Although the skeletal elements have the same general kinematic motions at each wing joint, the timing and excursion angles differ, and so, are responsible for the different external wing kinematics. In the pigeon, the wingtip-reversal upstroke is largely dominated by high long-axis rotation (80°) at the wrist mid-way through the upstroke, and quick long-axis rotation of the humerus (98°) near the end of upstroke. In contrast, the flexed-wing upstroke of the starling is dominated by flexion of the ulna at the elbow joint.

One notable exception to all joints undergoing similar kinematic trajectories is in the long-axis rotation of the wrist. The starling wrist undergoes negligible long-axis rotation. The rotation that it does go through is in the opposite direction to that of the pigeon: the manus of the starling pronates slightly as the pigeon manus supinates at the start of the upstroke. This one difference appears crucial for the tip-reversal upstroke of the pigeon – in particular, the pronation of the primary feathers during the upstroke- to downstroke transition.

We find qualitative evidence that supports the hypothesis presented by Vazquez (1992), wherein pronation of the hand-wing during the tip-reversal upstroke is due to an interaction between the carpometacarpus and the ulnare (supplemental video 1). This video was accomplished with the assumption that the ulnare follows the general kinematic trajectory of it's more proximal element, the ulna/radius, and so is an approximation of wrist bone kinematics. With these

323 assumptions acknowledged, we observe that the carpometacarpus slides along the
324 ventral ramus of the ulnare. Further work to explore the relative contribution of the
325 distal muscular elements to this motion is necessary to validate Vazquez' (1992)
326 hypothesis that this motion is muscularly passive, and completely skeletally-driven.
327 Additionally, higher resolution studies with more wrist bone markers are necessary
328 to validate our assumption of ulnare motion.

329 Our kinematic observations for both birds are different from those reported
330 in the hummingbird. In hummingbirds, the wing inversion during transitions from
331 upstroke to downstroke and vice-versa is predominately due to action at the
332 shoulder joint (Hedrick *et al.* 2012). However, in both species studied here, much of
333 wing motion occurs in the more distal joints (elbow, wrist), as opposed to the
334 shoulder joint. Distal motion does rely on the humerus (Fig. 5, 6), but is not the sole
335 contributor to movement. In particular, long-axis rotation of the humerus occurs
336 over a very short period of time at the end of upstroke in the pigeon. This long axis
337 rotation was first observed in both pigeons and starlings based on *in vivo* muscle
338 stimulation studies (Poore *et al.* 1997), and from rotoscoping of the pigeon humerus
339 (Gatesy *et al.* 2010). This motion likely contributes to reorienting the secondary
340 feathers dorsally during an aerodynamically active "clap" phase, wherein the left
341 and right wing come in to contact and shed circulation from the wing (Crandell &
342 Tobalske 2015).

343 We found evidence that the skeletal elements of the bird wing do not lock in
344 to place during the downstroke –first proposed by Sy in 1936 (Sy 1936; Vasquez
345 1992). In particular, we observed significant motion in all degrees of freedom in

346 both species throughout the downstroke (Fig. 3, 4, 5). Examining wingtip-traces
347 once the effects of the most proximal element (humerus) are removed easily reveals
348 that a substantial amount of abduction, adduction, flexion, and extension occur at
349 the more distal joints. Additionally, substantial long-axis rotation is observable
350 during the downstroke in both the wrist of the pigeon (Fig. 3A) and elbow of both
351 species (Fig. 4A,D). This long-axis rotation may be due to aerodynamic loading of
352 the feathers, as it is in the proper direction if the wing is aerodynamically loaded
353 with the center of pressure behind the bones. If this is so, differences in the degree
354 of long-axis rotation may be due to smaller distal muscle masses in the starling, and
355 so less muscle work available to maintain proper wing orientation. Further work
356 examining distal muscle contribution to wing shape is necessary to elucidate the
357 role of the distal muscles relative to aerodynamic loading of the wing.
358 Further, timing and magnitude of wrist extension varies relative to elbow
359 extension, countering the idea of an automatic linkage system between limb
360 segments in bird wings (Vazquez 1994). In the pigeon, the elbow begins extending
361 approximately 10 milliseconds (or 8% of the length of a wingbeat cycle) before the
362 wrist extends in the pigeon (Fig. 3C, 4C). In the starling, the delay is 4% of the
363 wingbeat cycle4 between the initiation of elbow extension and wrist extension. In
364 the pigeon, the humerus begins extending after the extension of the elbow (11%)
365 and wrist (5%). Baier et al. (2013) have shown similar timing differences in chukar
366 partridges during ascending flight, but find timing similarities of limb extension in
367 chukar during wing assisted incline running. Here, we add that flexion distally in the
368 elbow and wrist occur before flexion at the humerus. This timing difference in the

opposite direction that would be expected if the linkage system is lead by movements of proximal skeletal elements (i.e., the humerus). Together, this suggests that an "automatic linkage system" is not used during slow flight. Such a system may exist and be deployed during fast flight or gliding, wherein maintaining a relatively flat wing is crucial to force production. Further work examining the skeletal system under different flight speeds is necessary.

Our data reveal that there are stereotypical patterns of motion regardless of external wing kinematics. However, these patterns vary between species in terms of the excursion angles and timing of actions. As skeletal kinematic patterns are similar across species, this suggests that the underlying muscles of the wing may operate under a central pattern generator (Brown 1911; Kiehn 2006), with muscle activation timing and magnitude modified over evolutionary time. Alternatively, muscles may have been co-opted to perform different locomotor tasks. Further work examining precise muscular control of wing morphing is necessary to elucidate the underlying control mechanisms (Dial 1992a).

Kinematic data illustrate that external wing (and feather) kinematics are driven by underlying skeletal motion, and not just passive aerodynamic or other kinetic aspects, such as inertia of the wing. The wingtip-traces for both species (Fig. 6B, 7A), largely reflect the three-dimensional wingtip traces of the distal-most point of the 10^{th} (or 9^{th}) primary feather previously reported. To compare feather- to skeletal- motion, we compare our data to several sources of external kinematic data. Three-dimensional kinematics for the pigeon have been previously reported (Berg

392 & Biewener 2008; Berg & Biewener 2010) alongside two-dimensional kinematics of
393 the pigeon (Tobalske & Dial 1996). Tobalske & Dial (1996) have also reported two-
394 dimensional kinematic data for the black-billed magpie, which closely matches
395 three-dimensional kinematic data reported for the Zebra finch in slow flight
396 (Crandell & Tobalske, 2015). Thus, we assume for the purposes of this discussion
397 that passerines (including the magpie, zebra finch, and the starling studied here)
398 have a characteristic wingstroke during slow flight.

399 When comparing our skeletal data to sources of external wing kinematics,
400 both pigeons and starlings include a higher abduction of the manus in comparison to
401 the feather trace. Intriguingly, the manus in the pigeon follows along an identical
402 lateral path during upstroke and downstroke. Feather tip-traces of a diamond dove
403 (and pigeon) show differences in the degree of flexion toward the mid-line of the
404 body, wherein the distal primary feather follows a figure-of-eight pattern. The
405 feather tip stays closer to the mid-line of the body during the first half of upstroke in
406 comparison to the wing tip trace during downstroke, while the feather tip is farther
407 from the body during the end of upstroke in comparison to the start of downstroke
408 (Figure 1 of Chapter 2; Crandell & Tobalske, 2015). We posit that the difference
409 between the skeleton and feather observed kinematics may be due to feather inertia
410 (Gatesy & Baier 2005) or aerodynamic loading (Chang *et al.* 2013; Crandell &
411 Tobalske 2015).

412 Here, we have established that external wing kinematics of birds in slow
413 flight are closely mirrored by internal skeletal kinematics. Further, all birds undergo
414 similar patterns of motion skeletally during slow flight. However, differences in

magnitude of joint excursion and timing contribute greatly to overall differences in wing motion.

Figures & Tables

Trunk:

Marker #	2	3	4
1	0.096	0.084	0.078

Humerus:

Marker #	6	7	8
5	0.092	0.17	0.0258

Manus:

Marker #	15	16	17	18
14	0.12	0.164	0.116	0.17

Table 1: Standard deviations (mm) for each marker pair on the same bone for pigeon WG during trial 7.

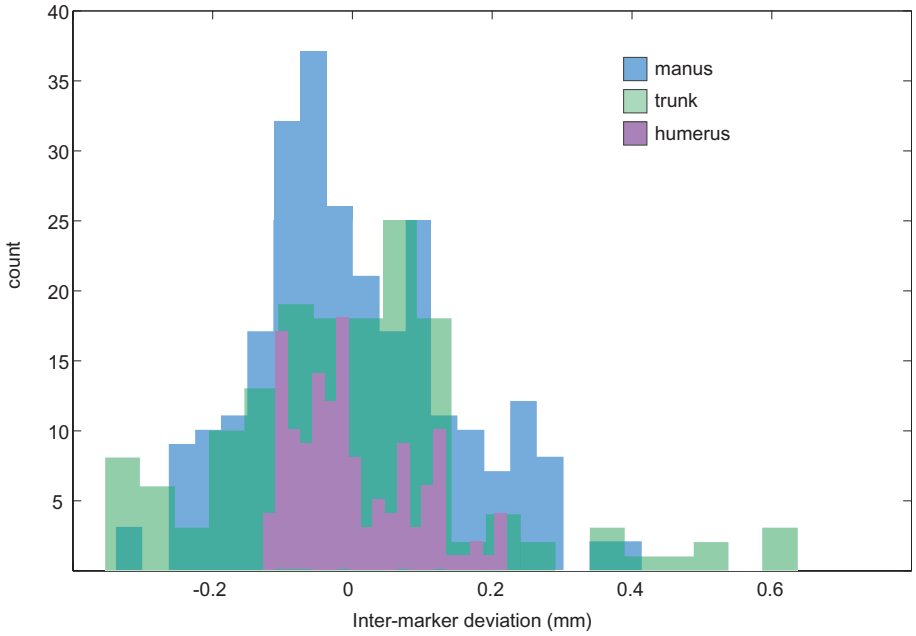

Figure 1: Histogram of deviations from the mean distance (0) between two markers on the same bone for pigeon WG, run 7. Blue histogram includes data from four marker pairs on the manus. The green histogram includes 4 marker pairs on the trunk, and purple includes 3 marker pairs of the humerus.

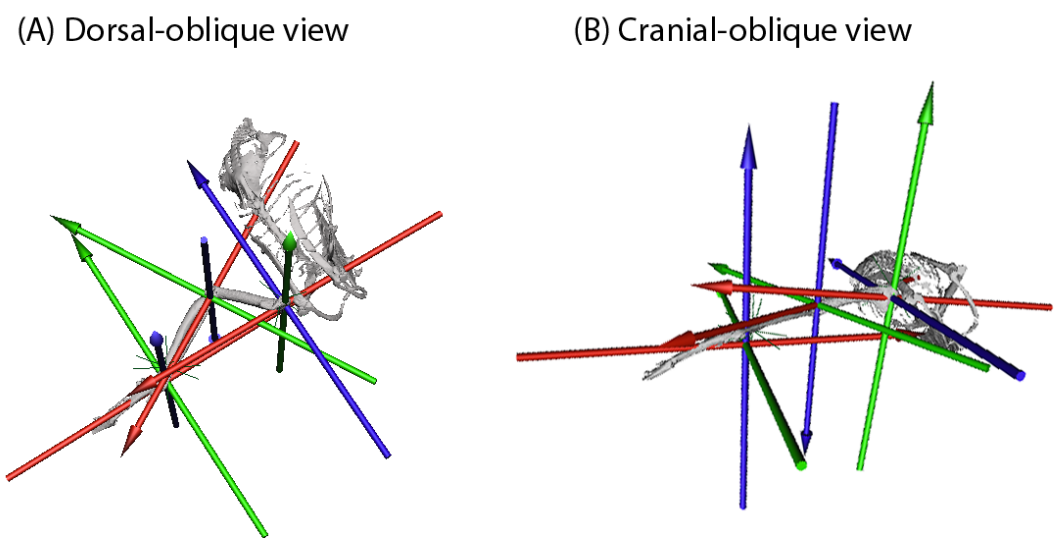

Figure 2: (A) Dorsal-oblique and (B) Cranial-oblique view of the Joint Coordinate System (JCS) for all species, shown on the starling. Herein, all reported values are relative to this mid-downstroke position (the 'zero position'). Each joint has six degrees of freedom based on inertial axes of the distal bone. Degrees of freedom are as follows for the wrist and elbow joint: Blue = abduction/adduction, Green = flexion/extension, Red = supination/pronation. For the Shoulder joint, blue = flexion/extension, green = abduction/adduction, red= supination/pronation

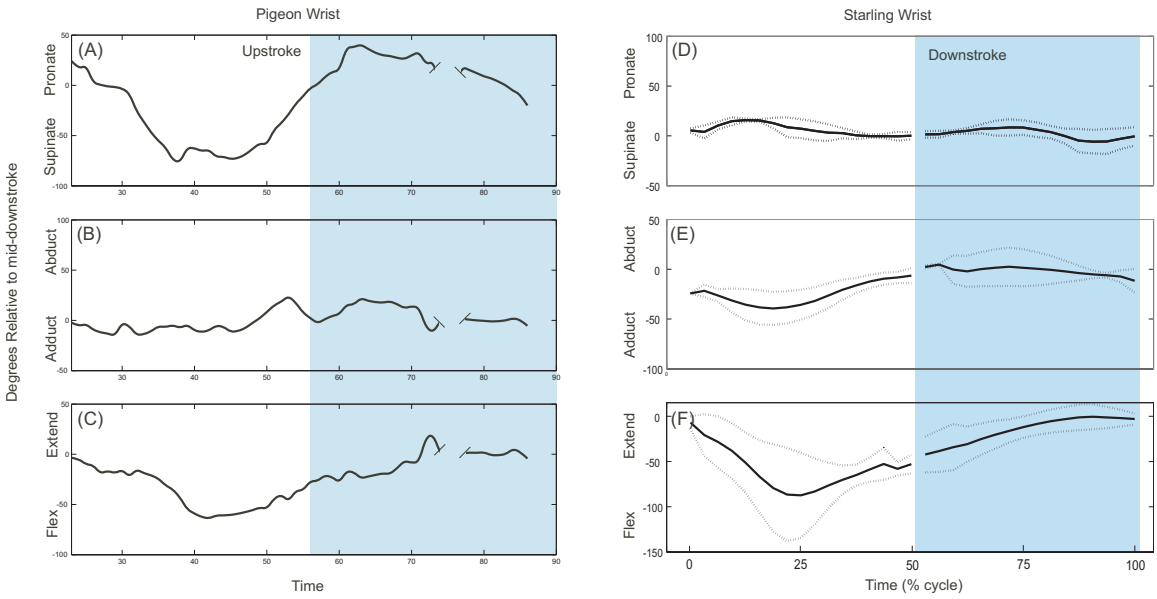

Figure 3: Representative trial for pigeon (A-C) and average (solid) ± s.d. (dashed) for starlings (n=3) (D-F). Each rotational degree of freedom for the wrist is shown. Line breaks in pigeon and starling represent missing data from stitching together of non-consecutive wingbeat segments.

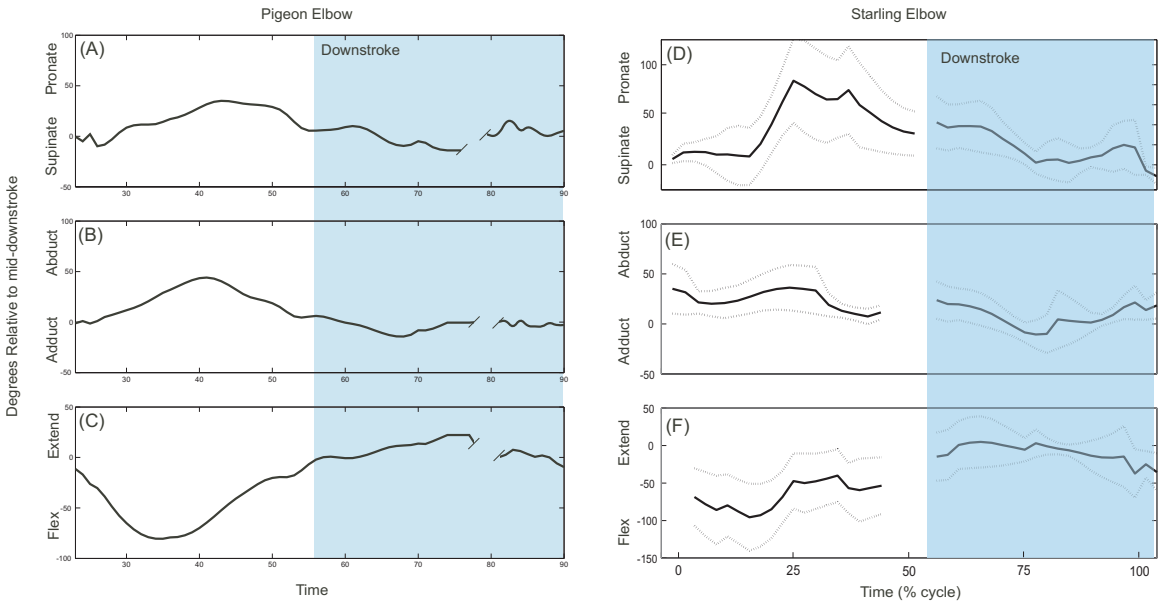

Figure 4: Representative trial for pigeon (A-C) and average (solid) ± s.d. (dashed) for starlings (n=3) (D-F). Each rotational degree of freedom for the elbow is shown.

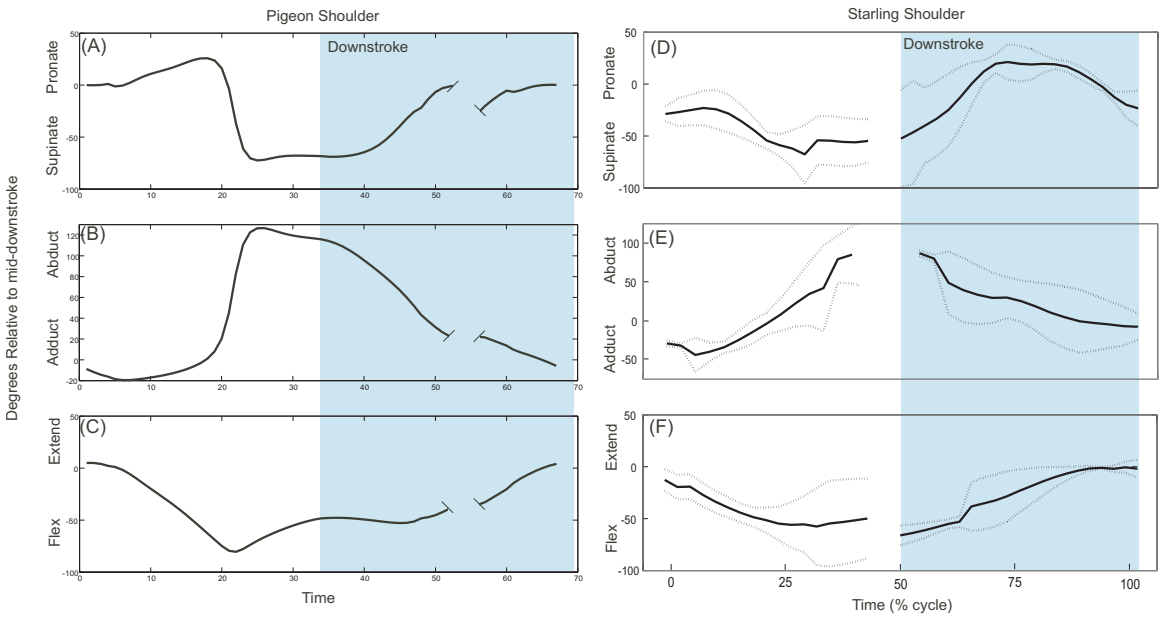

Figure 5: Shoulder joint coordinate kinematics for a representative wingbeat cycle for a pigeon (A-C) and average (solid) ± s.d. (dashed) for starlings (n=3) (D-F).

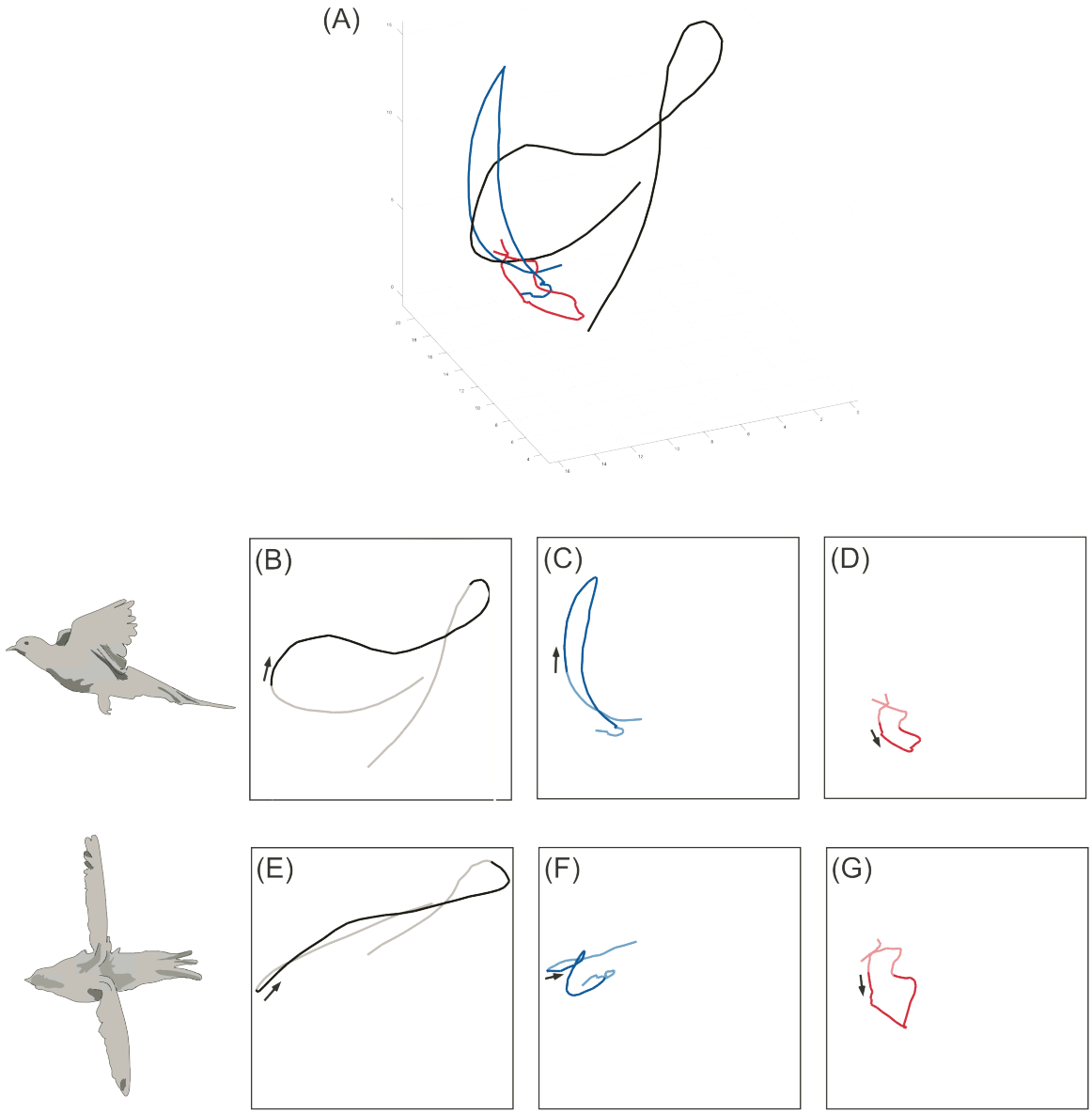

Figure 6: Traces of the distal-most point on the manus (phalanx 3) during a representative wingbeat cycle in the pigeon. Lighter colors represent the downstroke phase, darker colors represent the upstroke. Black arrows indicate the start of upstroke and the direction of wingtip motion. (A) illustrates a three-dimensional view of the wingtip path with each trace representing the motion due to different skeletal elements. (B-D) is a lateral view of the tip traces, and (E-G) is a dorsal view. For all graphs, black = shoulder-centered coordinates of the wingtip (including motion of the humerus, radius/ulna, and carpometacarpus), blue = elbow-centered coordinates (including motion of the radius/ulna and carpometacarpus), red = wrist-centered coordinates (including only motion of the carpometacarpus).

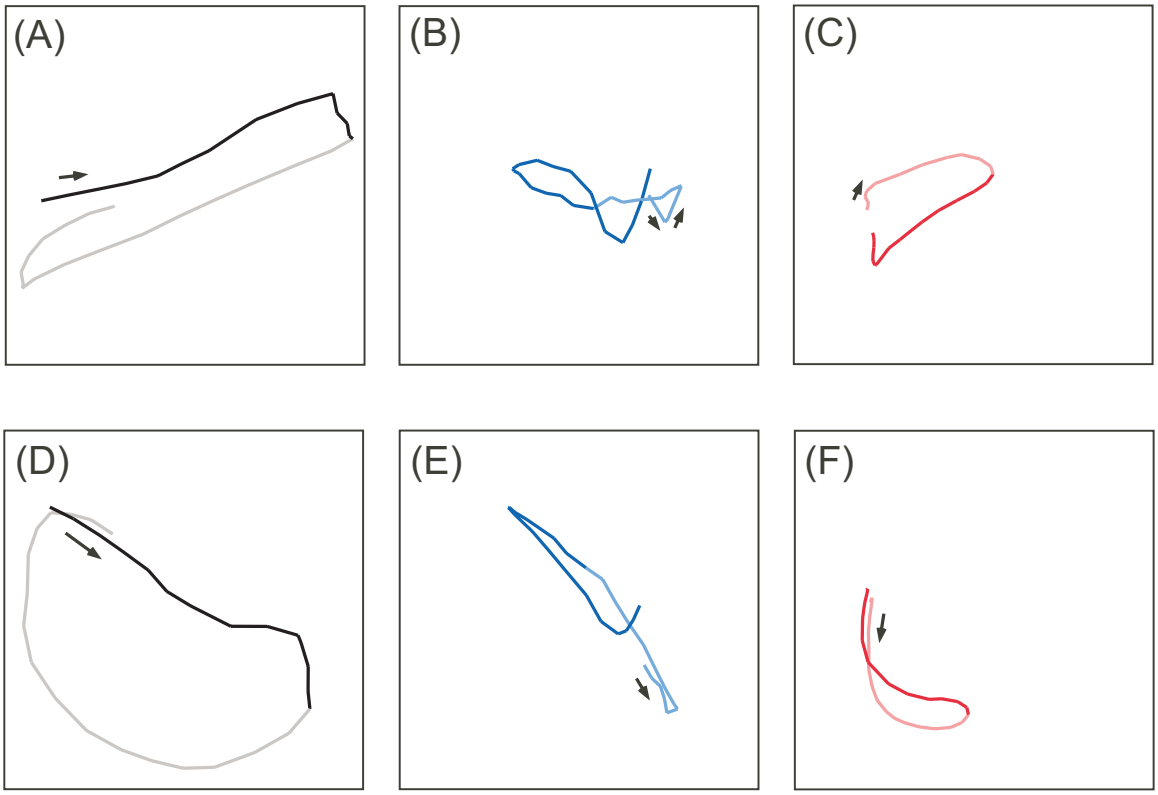

Figure 7: Traces of the distal-most point on the manus (phalanx 3) during a representative wingbeat cycle in the starling, flying to the left. Lighter colors represent the downstroke phase, darker colors represent the upstroke. Black arrows indicate the start of upstroke and the direction of wingtip motion. (A) illustrates a three-dimensional view of the wingtip path with each trace representing the motion due to different skeletal elements. (A-C) is a lateral view of the tip traces, and (D-F) is a dorsal view. For all graphs, black = shoulder-centered coordinates of the wingtip (including motion of the humerus, radius/ulna, and carpometacarpus), blue = elbow-centered coordinates (including motion of the radius/ulna and carpometacarpus), red = wrist-centered coordinates (including only motion of the carpometacarpus).

Acknowledgements

For assistance with surgical procedures, data collection, and/or insight toward XROMM, we thank Ashley Heers, Andy Biewener, Beth Brainerd, Bret Tobalske, Brandon Jackson, Cosima Schunk, Dave Baier, Heather Labbe, Ivo Ros, Kia Huffman, Pauline Provini, Robert Niese, and the XROMM short course staff. Additional thanks for the generosity of the Concord Field Station, including Pedro Ramirez and Ken Wilcox, for assistance with animal care and housing and preliminary data collection.

REFERENCES:

Baier, D.B., Gatesy, S.M. & Dial, K.P. (2013) Three-dimensional, high-resolution skeletal kinematics of the avian wing and shoulder during ascending flapping flight and uphill flap-running.

Berg, A.M. & Biewener, A.A. (2008) Kinematics and power requirements of ascending and descending flight in the pigeon (Columba livia). *Journal of Experimental Biology,* **211,** 1120-1130.

Berg, A.M. & Biewener, A.A. (2010) Wing and body kinematics of takeoff and landing flight in the pigeon (Columba livia). *Journal of Experimental Biology,* **213,** 1651-1658.

Brainerd, E.L., Baier, D.B., Gatesy, S.M., Hedrick, T.L., Metzger, K.A., Gilbert, S.L. & Crisco, J.J. (2010) X-Ray reconstruction of moving morphology (XROMM): Precision, accuracy, and applications in comparative biomechanics research. *J. Exp. Zool.,* **313A,** 262-279.

Brown, T.G. (1911) The intrinsic factors in the act of progression in the mammal. *Proceedings of the Royal Society of London. Series B, containing papers of a biological character***,** 308-319.

Chang, Y.-H., Ting, S.-C., Su, J.-Y., Soong, C.-Y. & Yang, J.-T. (2013) Ventral-clap modes of hovering passerines. *Physical Review E,* **87,** 022707.

Corvidae, E.L., Bierregaard, R.O. & Peters, S.E. (2006) Comparison of wing morphology in three birds of prey: Correlations with differences in flight behavior. *Journal of Morphology,* **267,** 612-622.

Crandell, K.E. & Tobalske, B.W. (2011) Aerodynamics of tip-reversal upstroke in a revolving pigeon wing. *Journal of Experimental Biology,* **214,** 1867-1873.

Crandell, K.E. & Tobalske, B.W. (2015) Kinematics and aerodynamics of avian upstrokes during slow flight. *The Journal of experimental biology***,** jeb. 116228.

Dial, K.P. (1992a) Activity patterns of the wing muscles of the pigeon (Columba-livia) during different modes of flight. *Journal of Experimental Zoology,* **262,** 357-373.

Dial, K.P. (1992b) Avian forelimb muscles and nonsteady flight - Can birds fly without using the muscles in their wings? *Auk,* **109,** 874-885.

Gatesy, S.M. & Baier, D.B. (2005) The origin of the avian flight stroke: a kinematic and kinetic perspective. *Paleobiology,* **3,** 382-399.
Gatesy, S.M., Baier, D.B., Jenkins, F.A. & Dial, K.P. (2010) Scientific Rotoscoping: A morphology-based method of 3-D motion analysis and visualization. *J. Exp. Zool.,* **313A,** [online advance].
Hedrick, T.L., Tobalske, B.W., Ros, I.G., Warrick, D.R. & Biewener, A.A. (2012) Morphological and kinematic basis of the hummingbird flight stroke: scaling of flight muscle transmission ratio. *Proceedings of the Royal Society B-Biological Sciences,* **279,** 1986-1992.
Kambic, R.E., Roberts, T.J. & Gatesy, S.M. (2014) Long-axis rotation: a missing degree of freedom in avian bipedal locomotion. *The Journal of experimental biology,* **217,** 2770-2782.
Kiehn, O. (2006) Locomotor circuits in the mammalian spinal cord. *Annu. Rev. Neurosci.,* **29,** 279-306.
Nudds, R.L. (2007) Wing-bone length allometry in birds. *Journal of Avian Biology,* **38,** 515-519.
Poore, S.O., Ashcroft, A., Sanchez-Haiman, A. & Goslow, G.E. (1997) The contractile properties of the M-supracoracoideus in the pigeon and starling: A case for long-axis rotation of the humerus. *Journal of Experimental Biology,* **200,** 2987-3002.
Sy, M. (1936) Funktionell-anatomische untersuchungen am vogelfl√ºgel. *Journal of Ornithology,* **84,** 199-296.
Tobalske, B.W. & Dial, K.P. (1996) Flight kinematics of black-billed magpies and pigeons over a wide range of speeds. *Journal of Experimental Biology,* **199,** 263-280.
Tobalske, B.W. & Dial, K.P. (2000) Effects of body size on take-off flight performance in the Phasianidae (Aves). *Journal of Experimental Biology,* **203,** 3319-3332.
Tobalske, B.W., Hedrick, T.L., Dial, K.P. & Biewener, A.A. (2003) Comparative power curves in bird flight. *Nature,* **421,** 363-366.
Vasquez, R.J. (1992) Functional osteology of the avian wrist and the evolution of flapping flight. *Journal of Morphology,* **211,** 259-268.
Vazquez, R.J. (1994) The automating skeletal and muscular mechanisms of the avian wing (aves) *Zoomorphology,* **114,** 59-71.
Vazquez, R.J. (1995) Functional anatomy of the pigeon hand (Columba livia): a muscle stimulation study. *Journal of Morphology,* **226,** 33-45.

Chapter 4

Coping with compliance during take-off and landing in the diamond dove (*Geopelia cuneata*)

Kristen E Crandell*[,1], Austin F. Smith, Ondi Crino[2], Bret W. Tobalske[1]
1. Field Research Station at Fort Missoula, Division of Biological Sciences, University of Montana, Missoula, MT USA.
2. Centre for Integrative Ecology, Deakin University, Victoria, Australia

*author for correspondence (kristen.crandell@gmail.com)

Abstract

Structural variation in natural habitats imposes constraints on locomotor performance. Birds appear to transition smoothly from aerial to terrestrial environments during take-offs and landings, however, these transitions are likely challenged by perch compliance (the opposite of stiffness). Given the ecological ubiquity of substrate variation, here we examine how birds modulate their performance during take off and landing on substrates of low, medium, and high compliance. We find birds do not capitalize on perch compliance, and so in general suffer from inefficient transitions. In particular, take-off velocities are negatively impacted by perch compliance, and landing velocities remain unchanged. Legs and wings function as independent units, such that lower initial flight velocity due to the legs negatively impacts later flight velocities. During landing, significant stability problems arose with compliance that were ameliorated by the wing and tail modules. Lastly, we find evidence for wild birds behaviorally avoiding the negative impacts of compliance by using perches of larger diameter.

Introduction

Natural habitats are full of structural variation that imposes constraints upon locomotor performance. Vegetation varies in orientation, roughness, size, and compliance. For example, the flexural stiffness of branches varies 4-fold within a single genus of trees in a single forest (van Casteren *et al.* 2013). Such variation can directly impact locomotor capacity. As an example, a slight change in the angle of a substrate (from 0 to +10 degrees) caused a 46% decrease in running velocity in geckos that had their adhesive system deployed (Russell & Higham 2009).

Substrate compliance (i.e., flexibility, or the opposite of stiffness) poses a unique challenge. As an organism moves, it transfers kinetic energy from itself to the substrate, which is stored as potential energy. Unless that potential energy is recovered, this results in lower sum energy for the animal to engage in the pendular mechanics of walking or effectively launch from the substrate during running and leaping (Alexander 1991). Shape, diameter, and length play a role in the compliance of substrates (Vogel 2003). Given the high degree of variation, it is reasonable to predict that organisms have adapted a diverse set of strategies to accommodate structural compliance within the habitat.

Response to substrate compliance appears to vary among species. Orangutans, for example, are capable of capitalizing on whole-tree compliance by using trees as an "external spring:" converting the potential energy of the tree into kinetic energy to move across the canopy (Thorpe, Crompton & Alexander 2007). However, in Anolis lizards, compliant perches constrain initial jump velocity

(Gilman *et al.* 2012). Anoles appear to behaviorally adjust with preferences toward stiffer substrates (Gilman & Irschick 2013).

Reactions to compliance may differ between terrestrial and volant organisms. Shifting between a terrestrial and aerial environment appears seamless for many flying birds, yet is understood to be expensive in terms of power (Tobalske *et al.* 2003). In birds, take-off and landing offer instances of high selective pressure. In many species, escape from predation, mate courtship, and foraging rely on an accurate take-off. A precise and rapid landing is also crucial to avoid wing or whole-body damage and to minimize energy expenditure. Thus, the logical prediction that follows is that birds should take-off and land as quickly as possible to minimize energy expenditure and avoid damage.

To maximize safety and minimize energetic costs during transitions between substrates and air, it was formerly thought that anatomical and physiological wing and leg modules in birds, which operate independently during terrestrial and aerial locomotion, instead function in tandem during transition stages (Gatesy & Dial 1996). However, recent work has established that during take-off, the legs and wings continue to function discretely in certain species. The legs contribute most to initial acceleration in take-off, and the wings follow with significant forces only after the feet leave the substrate (Provini *et al.* 2012). During landing, the wings contribute the majority of the deceleration prior to leg interaction with the substrate (Provini *et al.* 2014). Control requirements during these phases are potentially challenged by large variation in compliance of natural perches. Little is known concerning how birds accommodate such a variety of structures during

79 transitions in spite of how this ties together the ecology of these animals with their
80 primary locomotor style.
81 During take-off, birds do not appear to adjust their leg forces to
82 accommodate variation in perch compliance (Bonser, Norman & Rayner 1999).
83 However, two other adjustments may occur to maximize take-off velocity. The first
84 is that birds may adjust the timing over which the force is applied. As velocity =
85 (force * time) / mass, if force remains constant, the remaining variable that can be
86 adjusted for greater velocity is time. In contrast, volant organisms may compensate
87 for lost performance from the hindlimbs in flight. Birds are known to modulate their
88 force production following take-off by engaging their wings to different degrees
89 (Provini *et al.* 2012). Therefore, even if energy is lost to the perch, causing a lower
90 initial jump velocity (as suggested in European Starlings; (Bonser, Norman & Rayner
91 1999)), volant organisms may be able to adjust in flight.
92 During landing, the leg forces are smaller than those during take-off (Provini
93 *et al.* 2012; Provini *et al.* 2014). In comparison to terrestrial organisms, aerial
94 landings capitalize on aerodynamic decelerations prior to landing, and so impact
95 forces are lower. As such, volant organisms may be able to prepare prior to landing
96 to accommodate variation in substrate properties. Pigeons approach a novel perch
97 at a much lower flight velocity than a well-known perch (Green & Cheng 1998),
98 suggesting that variation in preparation for landing on known substrates occurs in
99 birds.
100 Given the ecological significance of compliant substrate use and the
101 differences between the forces produced during take-off and landing in terrestrial

and aerial organisms, we decided to examine how perch compliance affects multiple aspects of take-off and landing in the diamond dove (*Geopelia cuneata*). Here, we address the following questions: (1) How are take-off and landing velocities impacted by perch compliance? (2) Do birds coordinate leg and wing modules to accommodate perch compliance? (3) Do birds select perches to avoid or enhance potential effects of compliance?

Methods

Perch Use

Five diamond doves (*Geopelia cuneata*) were trained to fly horizontally in the laboratory between two perches two meters apart. During training, birds randomly experienced each of three perch types daily for two weeks prior to data collection.

During experiments, perches were mounted to a custom 3-axis force plate (Bertec). We varied perch compliance (the opposite of flexural stiffness) using wood (flexural stiffness, EI=0.39 Nm^2), aluminum (EI=2.12 Nm^2), or steel (EI = 6.14 Nm^2) perches, each 5 mm in diameter. Estimated deflection for these perches, with a 50 g bird perched at the takeoff location, 40 cm from the point of attachment, were 2.6 cm, 0.5 cm, and 0.2 cm, respectively. During recorded trials, birds were given five to ten practice transitions on each substrate prior to data recording, intending to re-familiarize them with the substrate. Ten trials were collected per substrate, per bird, for both take-off and landing (60 trials total per bird). The order substrates were

used was randomized for each bird, but to allow for any known learning effects, perch type was not changed between the ten trials on each substrate.

From the force traces, we extracted resultant velocities (m s^{-1}), peak forces (N), and time (s) of force application. Time of force application was measured between the time after countermovement (when vertical force is less than body weight (Earls 2000; Provini *et al.* 2012)) and the time the bird's feet were off the perch, confirmed visually in high-speed video. During landing, low-frequency oscillations made suspect any measurements of instantaneous forces, but measuring timing to stability was feasible.

To measure wing contributions to accelerations and decelerations in body velocity, a high-speed video (Photron 1024 PCI) was taken laterally at 1,000 fps (shutter speed = 1/10,000). To test for wing recovery following takeoff, we measured flight velocity during the third complete wingbeat of flight. To test for potential wing use variation between substrates in preparation for landing, we also measured the flight velocity during the final complete wingbeat before landing.

Habitat Use Measurements

To measure perch selection versus availability in the wild, birds were observed at Philip Creek Cattle Station (Philip Creek, Northern Territory, Australia), and Burt Plain Cattle Station (Tanami Road, Alice Springs, Northern Territory, Australia). Doves were located with in response to visual and auditory cues. When a perched diamond dove was first encountered, the following information of the

initial sighting was recorded: perch diameter and distance to fulcrum (determined as distance to an intersecting branch/trunk >5 cm in diameter, or the visually-identified main stalk of the plant). To compare bird sightings to available habitat, 10 photographs were taken of surrounding habitat, and diameters and distances to fulcrum were measured in ImageJ for 200 randomly selected points.

Data analysis

To test for differences in performance parameters between substrate type, we used a within-subjects, repeated-measures ANOVA, with individual bird as a factor. To compare available vs. used habitat type, we used a t-test.

Results

We found that performance varied with perch compliance during both take-off and landing.

Take-off

Take-off velocities were lower with more compliant perches. Takeoff resultant velocities were significantly greater on the perch with the lowest compliance, steel (Figure 1A; ANOVA within-subjects factor $F_{2,8}=22.26$, $p<0.01$). Resultant velocities produced during take-off from aluminum and wood perches were less, and not statistically different from each other. Birds produced a velocity of 0.50 ± 0.12 ms^{-1} taking off from wood, followed by 0.53 ± 0.11 ms^{-1} from the aluminum perch, and 0.82 ± 0.21 ms^{-1} from the steel perch. We did not find that timing of force application changes with substrate compliance, indicating that birds

do not adjust force or timing of force application to improve take-off velocity in response to perch compliance. However, a general trend toward longer force application times was apparent, although not statistically significant ((Figure 1B; $F_{2,8}$=1.89, p=0.21; wood = 0.05 ± 0.02 s, aluminum = 0.06 ± 0.01 s, steel = 0.07 ± 0.02). Additionally, we did not find evidence that birds utilized perch recoil to recover potential energy from the perch as kinetic energy. In all instances, the bird lost contact with the perch prior to the perch recoiling (Supplemental Video 1). Birds did appear to compensate for velocity lost on compliant substrates during take-off in flight. However, by the third wingbeat in flight, velocity lost via the legs due to perch compliance remained statistically significant: doves taking off from a wood perch had an in-flight velocity of 1.40 ± 0.34 ms^{-1}, take-off from an aluminum perch had a flight velocity at 1.46 ± 0.26 ms^{-1}, and following steel at 1.59 ± 0.25 ms^{-1} (Figure 1C; $F_{2,8}$ = 12.04, p<0.01).

Landing

During landing, we found that birds approach perches at constant velocities, with statistically non-significant differences ($F_{2,4}$ =1.36, p=0.35), regardless of perch compliance (Figure 2). This negates the idea that birds prepare for landing to capitalize on the physical properties of known substrates. In contrast, we found that stabilization and control were greatly challenged on compliant substrates during landing.

Upon landing, we saw predictable patterns of body reorientation. At touch-down, the bird immediately adjusts to a more upright posture, and then folds the

193 wings – as observed upon landing on the substrate with minimal-compliance, steel
194 (Figure 3A, steel). During this reorientation phase, the bird initially touches down at
195 a body angle between the eye and rump of 26.3 ± 45.8° from horizontal. The bird
196 then reorients to a resting angle of 70.4±2.8° from horizontal. During the
197 reorientation phase, the bird peak angular velocity of reorientation occurs at 50
198 milliseconds after touch-down, at 11.4±3.3 rad s^{-1}.

199 A failure in stability, then, can be quantified when this reorientation is
200 delayed or variable. In both wood and aluminum treatments, birds took
201 considerably longer to reach stability, and showed high standard deviations in the
202 timing of stability (Figure 3B and 3C). Further, additional changes in angular
203 velocity before and after stability indicate failed attempts or drastic posture changes
204 in order to gain stability. During landings on wood, we found many small angular
205 velocity peaks – the first 4.8±4.0 rad s^{-1} at approximately 50 milliseconds following
206 touchdown, then 7.4 ± 4.2 rad s^{-1} at 150 milliseconds, and again 5.4±1.9 rad s^{-1} at
207 250 milliseconds, and finally at 4.3±2.1 rad s^{-1} at 410 milliseconds. During the final
208 three angular velocity peaks, body angle relative to horizontal varied between 52.9°
209 and 83.0°. During landings on aluminum, small peaks in angular velocity were
210 apparent as well, at 7.6± 2.4 rad s^{-1} at 40 milliseconds after touchdown, again at
211 12.1±3.2 rad s^{-1} at 130 milliseconds, and 6.0±2.3 rad s^{-1} at 330 milliseconds. During
212 the final two angular velocity peaks, the body angle varied between 63° and 84°.

213 We found that there is a difference between time-to-stabilization between
214 substrate treatments (Figure 4; $F_{2,8} = 4.21$, $p = 0.056$). On wood substrates, birds are
215 stable at 213 ± 134 ms following touch-down, on aluminum, 151 ± 99 ms, while

stabilization on steel occurred at 109 ± 26 ms following touch-down. The large standard deviations among substrate treatment indicate challenges of gaining control. In contrast, we found no significant differences among perch types for timing of leg extension prior to landing, which we assumed as an additional proxy for landing preparation (Figure 3D; $F_{2,8}$ =0.59, p=0.58).

In addition to variation in control, we found that doves had stereotypical countermovements following landing, to aid in stability. Birds generally (74%) used their tail as a ventral counter weight (Figure 5A & 5B), flexing the tail ventrally under the perch to help counter the rotational motion of the body. In 26% of the trials, the birds used their tails in the opposite fashion, extending them dorsally over their heads and vertically above the perch (Figure 5A and 5C). This counter-weight function was observed most frequently on the wood perch (50% of the time), the most compliant substrate (Supplemental Video 2), followed by 17% of the time when landing on aluminum, and 10% of the time when landing on steel. Within each class of countermovement, the angle between the bird's body and tail did not differ significantly among substrates (tail-down: $0.17<p<0.94$, tail-up: $0.78<p<0.98$; Figure 5A).

Perch Preference

We found significant differences between perch diameters available in the habitat and the perch diameter upon which diamond doves were found in the wild (t-test $p<0.01$); Figure 6). Birds were found on perches averaging 2.27 ± 1.42 cm in diameter, with a median value of 1.72 cm (n=25; Fig. 5A). The smallest perch found

in-use was 0.87 cm in diameter, and the largest was 5.4 cm. In contrast, the average perch available in the habitat was 0.85 ± 1.42 cm in diameter. The minimum diameter observed was 0.06 cm in diameter, while the maximum was 8.54 cm. Birds were observed on average 73.8 ± 55.1 cm from the nearest fulcrum within a shrub or tree.

Discussion

Variation in perch compliance impacts both take-off and landing abilities. Birds do not appear to capitalize on perch compliance during transitions, and as such, appear to suffer from inefficient transitions. Addressing our original questions, we found that take-off velocities are negatively impacted by perch compliance, while landing velocities remain unchanged. Additionally, we found minimal support for module coordination between the legs and wings during take-off. Instead, we found independent use of the modules, such that lower initial velocity due to the legs impacted later flight velocities, and during landing the wing and tail modules were used to aid in stabilization. Lastly, we found evidence for wild birds preferentially selecting perches of larger diameter, potentially minimizing effects of compliance during locomotor transitions.

Compliance impacts velocity during take-off

We found that take-off velocities are impacted negatively by perch compliance, while landing flight velocities are unaffected. During takeoff, birds lost energy to the substrate that they did not recover. We found no evidence that birds

modulate leg function to adjust for perch compliance; birds did not adjust the timing of force production (Figure 1B) or take-off force (Bonser, Norman & Rayner 1999). Thus, perches with higher compliance showed a lower instantaneous velocity at toe-off. Mathematical models of humans, bush-babies, and insects suggest that altering kinematic strategies on substrates of various compliance can dramatically change the resulting jump height (Alexander 1995). However, we saw no evidence for altering force-application timing during take-off in the doves. Both anole lizards (Gilman *et al.* 2012) and click-beetles (Ribak, Reingold & Weihs 2012) also do not alter force application to account for substrate variation.

Wing & leg modules function independently

Wing and leg modules were found to not function within the same time interval, as previously predicted by Gatesy and Dial (1996). During take-off, the legs lose energy to the perch, causing initial low velocities. Following take-off, the wings increase flight velocity, but flight velocity by the third wingbeat remains inhibited by the initial lower velocities on compliant substrates. During landing, the wings decelerate birds to a consistent flight velocity before touch-down. However, following touchdown, both the wings and the tail (a third module) assist in counterbalancing the body to improve stability. Neurological or musculo-skeletal limitations offer a hypothesis to explain the staggering of module timing, as well as the inability to compensate for perch compliance. Transitions may be constrained by a neurological central pattern generator (Brown 1911; Kiehn 2006), wherein the timing between leg- and wing-modules cannot be adjusted. Further work exploring

285 the neurobiology behind modules is necessary to improve our understanding of
286 potential neuromechanical limitations.
287 For birds, perfect force application during take-off via the legs may not be
288 crucial, as the wings take over immediately following loss of contact with the ground
289 (Provini *et al.* 2012). The dominant flight muscle, the pectoralis, produces the
290 highest known power output within vertebrate locomotion (Schmidt-Nielsen 1972).
291 Recent studies have established that the aerodynamic forces produced during
292 energetically demanding slow flight (Tobalske *et al.* 2003) are modulated (Provini et
293 al., 2012, 2014; Jackson, Tobalske & Dial 2011) such that even during the most
294 energetically demanding phase, power output can be adjusted depending on
295 acceleration requirements. As such, it is arguable that the avian wing musculo-
296 skeletal system is relatively 'overbuilt' in comparison to the leg, and so, is more
297 capable of adjusting and compensating during transitions than the legs. While this is
298 not observed in our data, we believe that had we extended the time interval over
299 which we sampled flight velocity (i.e., not immediately following take-off), flight
300 velocities would be indistinguishable between treatments.
301
302 *Birds show perch use preferences*
303 We found evidence that birds behaviorally adjusted for potential transitions
304 by preferentially selecting larger-diameter perches that were further from the
305 fulcrum compared with the distance to fulcrum in our laboratory tests (Figure 6).
306 This may aid in compensating for inefficient transitions we have reported on highly
307 compliant substrates (Figure 2, 3). Consistent with our assumption that stiffer

perches are better for high velocity take-off and better landing control, doves seem to prefer larger-diameter, stiffer branches in the wild. Further comparative work is warranted to examine the generalities of perch use in birds, alongside detailed habitat characteristic quantification (such as Gilman & Irschick, 2013).

Birds used in the laboratory study were raised in indoor aviaries with unlimited food supply and no predation pressure. Captive birds were not likely to be motivated to maximize performance in takeoff or landing, so caution is warranted when applying the results to an understand of transitions between substrates and the air in the wild. While the transitions we measured here did not optimize for variation in perch compliance, all birds completed their transitions without injury. During take-off, birds were able to accelerate in flight to equivalent speeds. During landing, birds all decelerated and reached stability successfully. As such, while the transitions were not efficient, they were effective. Further comparative studies are necessary to understand if inefficient transitions are a general character of birds, due to their powerful flight abilities.

FIGURES

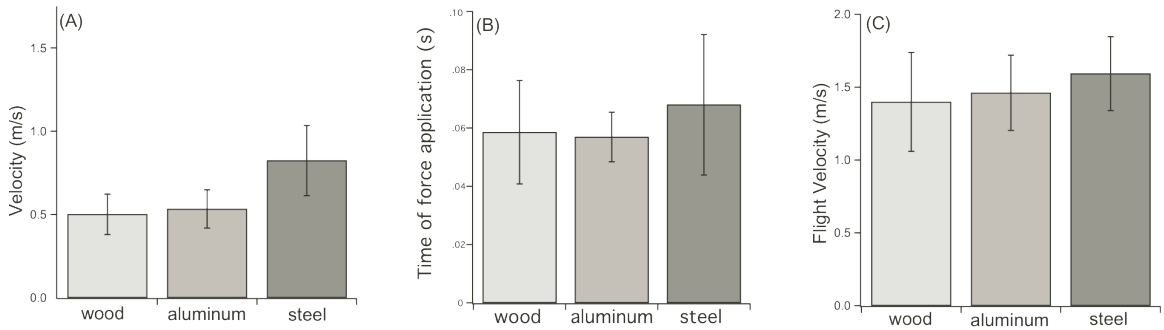

Figure 1: Take-off performance on perches of various compliance. Wood was the most compliant, steel, the least. (A) Resultant velocities at takeoff due to the legs (B) Timing of force application during take-off, (C) velocities at the third wingbeat of flight after toe-off.

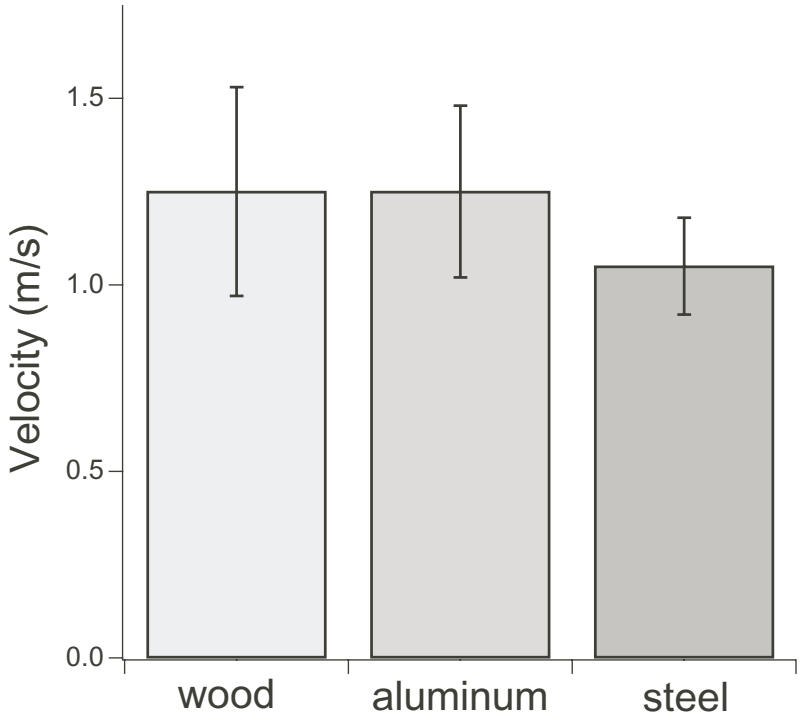

Figure 2: Flight velocities of the bird during the last complete wingbeat prior to landing for all three perch types.

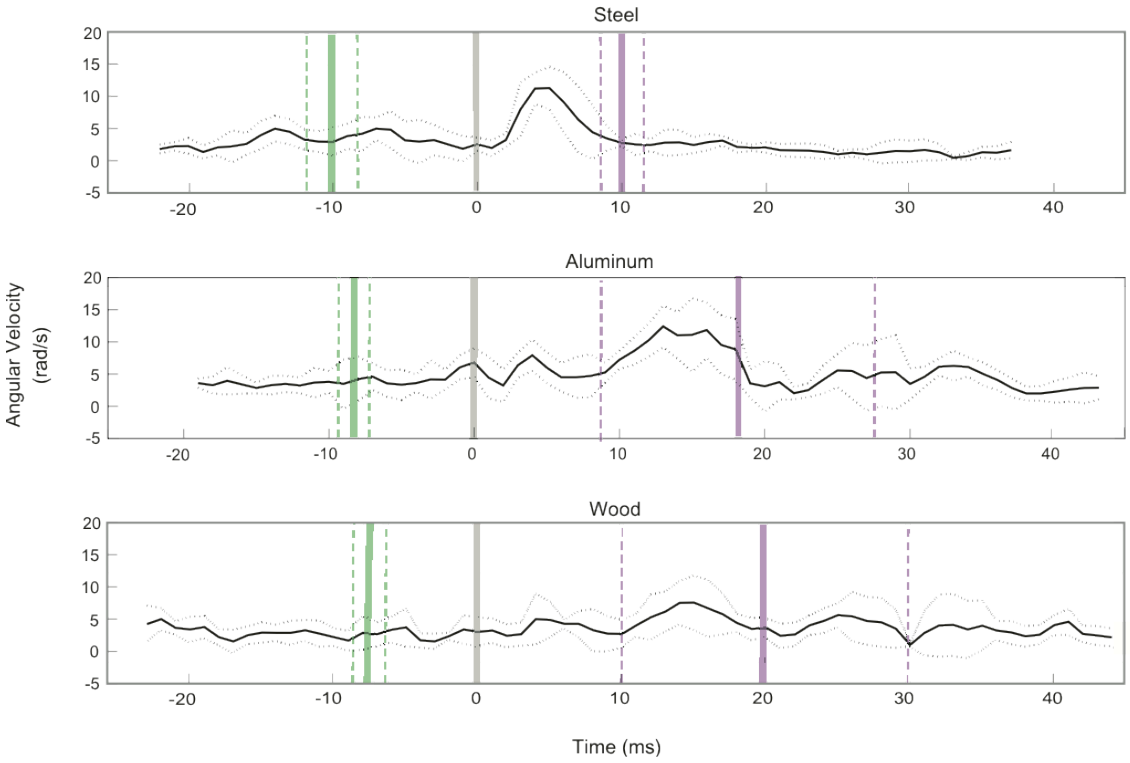

Figure 3: (A) Average angular velocities for ten trials of a representative individual (Dove 46) during landing on different substrates. Average timing (solid line) +/- standard deviation (dashed lines) is noted for foot extension (green), landing (gray), and the point the bird is considered stable (purple), following body reorientation. Instabilities are notable in following landing on the compliant substrates (aluminum and wood), indicated by additional angular velocities.

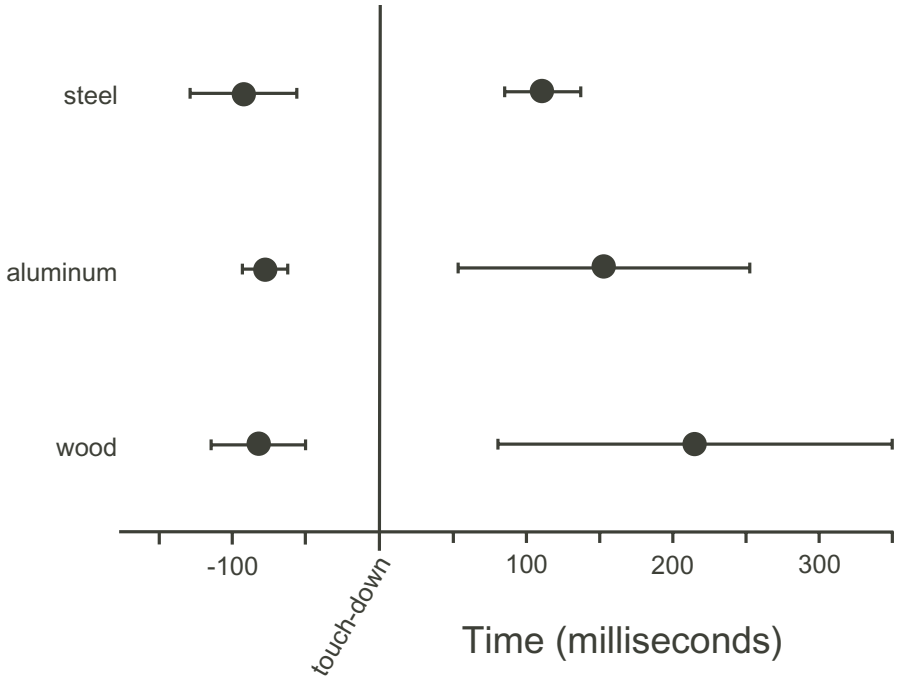

Figure 4: Timing of leg extension prior to landing (left) and point at which the bird has reoriented and is stable (right), relative to touchdown (time zero). Instabilities during landing are notable due to a longer time following touchdown and higher standard deviation until stabilization.

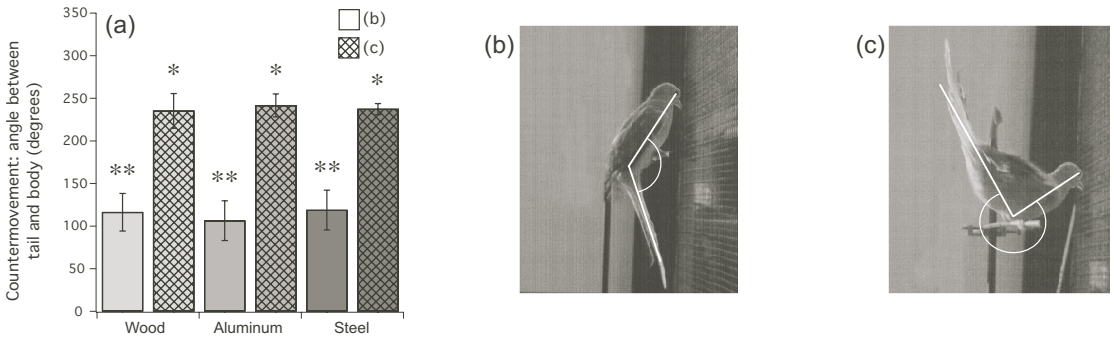

Figure 5: (A) Angle of countermovements during landing to aid in stabilization for both countermovement conditions. (B) An example of a tail-under countermovement, reaching an average angle of 113.7 ± 23.6 degrees. Between substrates, tail-under countermovements were statistically indistinguishable ($0.17 < p < 0.94$) (C) An example of a tail-over countermovement, reaching an average angle of 237.0 ± 17.4 degrees. Between substrates, tail-over countermovements were indistinguishable ($0.78 < p < 0.98$).

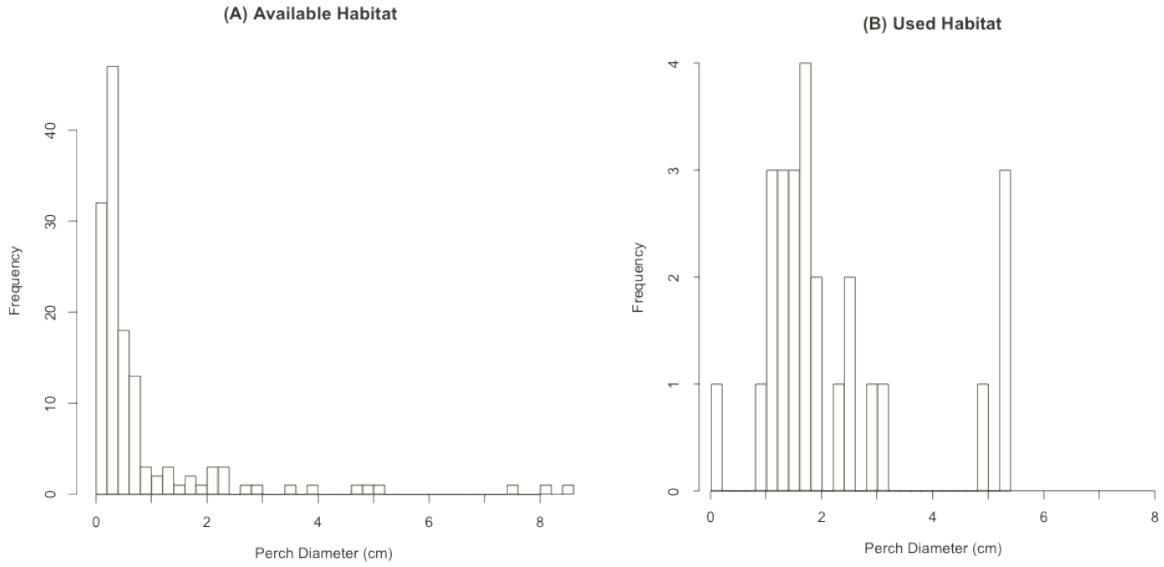

Figure 6: Perch use in native Diamond doves. (A) Perch diameters available within the habitat (B) Diameters of perches where doves were observed.

References:

Alexander, R.M. (1991) Elastic mechanisms in primate locomotion. *Zeitschrift f√ºr Morphologie und Anthropologie*, 315-320.

Alexander, R.M. (1995) Leg design and jumping technique for humans, other vertebrates and insects. *Royal Society Philosophical Transactions Biological Sciences,* **347,** 235-248.

Bonser, R.H.C., Norman, A.P. & Rayner, J.M.V. (1999) Does substrate quality influence take-off decisions in Common Starlings? *Functional Ecology,* **13,** 102-105.

Brown, T.G. (1911) The intrinsic factors in the act of progression in the mammal. *Proceedings of the Royal Society of London. Series B, containing papers of a biological character*, 308-319.

Earls, K.D. (2000) Kinematics and mechanics of ground take-off in the starling Sturnis vulgaris and the quail Coturnix coturnix. *Journal of Experimental Biology,* **203,** 725-739.

Gatesy, S.M. & Dial, K.P. (1996) Locomotor modules and the evolution of avian flight (vol 50, pg 331, 1996). *Evolution,* **50,** 2563-2563.

Gilman, C.A., Bartlett, M., Gillis, G. & Irschick, D. (2012) Total recoil: perch compliance alters jumping performance and kinematics in green anole lizards (Anolis carolinensis) (vol 215, pg 220, 2012). *Journal of Experimental Biology,* **215,** 568-568.

Gilman, C.A. & Irschick, D.J. (2013) Foils of flexion: the effects of perch compliance on lizard locomotion and perch choice in the wild. *Functional Ecology,* **27,** 374-381.

Green, P.R. & Cheng, P. (1998) Variation in kinematics and dynamics of the landing flights of pigeons on a novel perch. *Journal of Experimental Biology,* **201,** 3309-3316.

Jackson, B.E., Tobalske, B.W. & Dial, K.P. (2011) The broad range of contractile behaviour of the avian pectoralis: functional and evolutionary implications. *Journal of Experimental Biology,* **214,** 2354-2361.

Kiehn, O. (2006) Locomotor circuits in the mammalian spinal cord. *Annu. Rev. Neurosci.,* **29,** 279-306.

Provini, P., Tobalske, B., Crandell, K. & Abourachid, A. (2012) Transition from leg to wing forces during take-off in birds. *The Journal of experimental biology,* **215,** 4115-4124.

Provini, P., Tobalske, B.W., Crandell, K.E. & Abourachid, A. (2014) Transition from wing to leg forces during landing in birds. *The Journal of experimental biology*, jeb. 104588.

Ribak, G., Reingold, S. & Weihs, D. (2012) The effect of natural substrates on jump height in click-beetles. *Functional Ecology,* **26,** 493-499.

Russell, A.P. & Higham, T.E. (2009) A new angle on clinging in geckos: incline, not substrate, triggers the deployment of the adhesive system. *Proceedings of the Royal Society of London B: Biological Sciences,* **276,** 3705-3709.

Schmidt-Nielsen, K. (1972) Locomotion: energy cost of swimming, flying, and running. *Science,* **177,** 222-228.

Thorpe, S.K.S., Crompton, R.H. & Alexander, R.M. (2007) Orangutans use compliant branches to lower the energetic cost of locomotion. *Biology letters,* **3,** 253-256.
Tobalske, B.W., Hedrick, T.L., Dial, K.P. & Biewener, A.A. (2003) Comparative power curves in bird flight. *Nature,* **421,** 363-366.
van Casteren, A., Sellers, W.I., Thorpe, S.K., Coward, S., Crompton, R.H. & Ennos, A.R. (2013) Factors affecting the compliance and sway properties of tree branches used by the Sumatran orangutan (Pongo abelii). *PloS one,* **8**.
Vogel, S. (2003) Comparative Biomechanics: Life's physical world. Princeton University Press, Princeton, New Jersey.